

<b>1. Report No.</b> FHWA/TX-84/39+246-2	<b>2. Government Accession No.</b>	<b>3. Recipient's Catalog No.</b>	
<b>4. Title and Subtitle</b> DETECTION OF VOIDS UNDERNEATH CONCRETE PAVEMENTS USING INFRARED THERMOGRAPHY		<b>5. Report Date</b> June 1983	<b>6. Performing Organization Code</b>
<b>7. Author(s)</b> Mark E. Bukowski, Richard L. Tucker, and David W. Fowler		<b>8. Performing Organization Report No.</b> Research Report 246-2	
<b>9. Performing Organization Name and Address</b> Center for Transportation Research The University of Texas at Austin Austin, Texas 78712-1075		<b>10. Work Unit No.</b>	<b>11. Contract or Grant No.</b> Research Study 3-18-79-246
<b>12. Sponsoring Agency Name and Address</b> Texas State Department of Highways and Public Transportation; Transportation Planning Division P. O. Box 5051 Austin, Texas 78763		<b>13. Type of Report and Period Covered</b> Interim	
<b>15. Supplementary Notes</b> Study conducted in cooperation with the U. S. Department of Transportation, Federal Highway Administration Research Study Title: "Polymer Concrete for Concrete Pavement Rehabilitation"		<b>14. Sponsoring Agency Code</b>	
<b>16. Abstract</b>  <p>This report describes preliminary theoretical and experimental investigations of a technique for void detection beneath concrete pavements. The technique is based upon use of infrared thermography and the hypothesis that the surface temperature of the pavement over the void is slightly different than the surface temperature of pavement in contact with the base material.</p> <p>Experimental investigations were conducted on a concrete slab 12 ft x 21 ft x 8 inches thick which was cast at Balcones Research Center. Three voids of known locations and dimensions were created beneath the slab. Thermistors were installed at various locations in the concrete slab and in the soil beneath the slab to monitor air, ground, and soil temperatures. An infrared scanning camera system was installed on a truck-mounted frame.</p> <p>Thermistor scans were conducted on five dates and an infrared scan was conducted on one date in late 1980. Results of the experimental studies show that thin voids can be detected by the infrared thermography technique. The technique is sensitive to environmental factors and needs additional investigation to determine optimum applications.</p>			
<b>17. Key Words</b>  voids, detection, concrete, pavements, infrared, thermography		<b>18. Distribution Statement</b>  No restrictions. This document is available to the public through the National Technical Information Service, Springfield, Virginia 22161.	
<b>19. Security Classif. (of this report)</b> Unclassified	<b>20. Security Classif. (of this page)</b> Unclassified	<b>21. No. of Pages</b> 116	<b>22. Price</b>

DETECTION OF VOIDS UNDERNEATH CONCRETE  
PAVEMENTS USING INFRARED THERMOGRAPHY

by

Mark E. Bukowski  
Richard L. Tucker  
David W. Fowler

Research Report Number 246-2

Research Project 3-18-79-246  
Polymer Concrete for Concrete Pavement Rehabilitation

Conducted for  
State Department of Texas Highways and Public Transportation

in cooperation with the

U.S. Department of Transportation  
Federal Highway Administration

by the  
Center for Transportation Research  
Bureau of Engineering Research  
The University of Texas at Austin

June 1983

The contents of this report reflect the views of the authors, who are responsible for the facts and the accuracy of the data presented herein. The contents do not necessarily reflect the official views or policies of the Federal Highway Administration. This report does not constitute a standard, specification, or regulation.

## PREFACE

This is the second report in a series of reports that describes the work done in Research Project 3-18-79-246, "Polymer Concrete for Concrete Pavement Rehabilitation." The report deals with preliminary investigations of efficient void-detection techniques.

Mark Bukowski  
Richard L. Tucker  
David W. Fowler

This page replaces an intentionally blank page in the original.

-- CTR Library Digitization Team

## ABSTRACT

This report describes preliminary theoretical and experimental investigations of a technique for void detection beneath concrete pavements. The technique is based upon use of infrared thermography and the hypothesis that the surface temperature of the pavement over the void is slightly different than the surface temperature of pavement in contact with the base material.

Experimental investigations were conducted on a concrete slab 12 ft x 21 ft x 8 inches thick which was cast at Balcones Research Center. Three voids of known locations and dimensions were created beneath the slab. Thermistors were installed at various locations in the concrete slab and in the soil beneath the slab to monitor air, ground, and soil temperatures. An infrared scanning camera system was installed on a truck-mounted frame.

Thermistor scans were conducted on five dates and an infrared scan was conducted on one date in late 1980. Results of the experimental studies show that thin voids can be detected by the infrared thermography technique. The technique is sensitive to environmental factors and needs additional investigation to determine optimum applications.

This page replaces an intentionally blank page in the original.

-- CTR Library Digitization Team

## SUMMARY

One of the primary factors that cause load failures in reinforced concrete pavements is nonuniform foundation support due to the presence of voids at the pavement/sub-base interface. A major problem in the treatment of voids is detecting them prior to pavement failure. A detection method which is both reliable and efficient is needed to cover the thousands of miles of highways in an efficient manner.

This report describes studies of void detection using infrared thermography. The studies were of a preliminary nature to determine the feasibility of the technique. An experimental section of a pavement slab was cast with voids of known locations and dimensions beneath it. The voids were detected by the infrared thermography process. Additional studies are recommended to further refine the process for prototype applications.

This page replaces an intentionally blank page in the original.

-- CTR Library Digitization Team

## IMPLEMENTATION

This study was of a preliminary nature only, and intended only to identify opportunities and needs for further investigations. Although the infrared thermography technique appears feasible for void detection, additional development of the method is needed prior to implementation on a broad scale.

This page replaces an intentionally blank page in the original.

-- CTR Library Digitization Team

## TABLE OF CONTENTS

	Page
PREFACE . . . . .	iii
ABSTRACT . . . . .	v
SUMMARY . . . . .	vii
IMPLEMENTATION . . . . .	ix
LIST OF TABLES . . . . .	xiii
LIST OF FIGURES . . . . .	xiv
 CHAPTER	
1 INTRODUCTION	1
1.1 Nature of the Problem . . . . .	1
1.2 Previous Studies in Infrared Detection of Voids . . . . .	3
1.3 Purpose of the Study . . . . .	6
1.4 Scope of the Study. . . . .	6
1.5 Organization of the Report . . . . .	7
2 THEORETICAL ANALYSIS	9
2.1 The Pavement Systems . . . . .	9
2.2 Thermal Model . . . . .	11
2.2.1 Parameters and Symbols . . . . .	12
2.2.2 Calculations of Surface Temperatures . . . . .	15
2.3 Radiation Balance Model . . . . .	18
2.4 Detection of Infrared Radiation . . . . .	21
3 DESCRIPTION OF EXPERIMENT	25
3.1 General Slab Dimensions . . . . .	25
3.2 Temperature Monitoring System . . . . .	27
3.2.1 Equipment . . . . .	27
3.2.2 Calibration . . . . .	31

CHAPTER	Page
3.3 Void Design . . . . .	33
3.4 Construction of Experimental Slab . .	38
3.5 The Infrared Scanning System . . . .	43
 4 EXPERIMENTAL RESULTS	 47
4.1 Temperature Data . . . . .	47
4.1.1 Scan Number 1 . . . . .	50
4.1.2 Scan Number 2 . . . . .	52
4.1.3 Scan Number 3 . . . . .	52
4.1.4 Scan Number 4 . . . . .	59
4.1.5 Scan Number 5 . . . . .	59
4.2 Results from Infrared Thermography .	59
 5 ANALYSIS OF RESULTS	 69
5.1 Thermistor Data . . . . .	69
5.1.1 Surface and Mid-depth Temperature Data . . . . .	 76
5.1.2 Soil Temperature Data . . . .	80
5.2 Thermal Imagery . . . . .	81
5.3 Correlation with Theory . . . . .	84
 6 CONCLUSIONS AND RECOMMENDATIONS . . . . .	 87
6.1 Conclusions . . . . .	87
6.2 Recommendations . . . . .	88
 APPENDIX . . . . .	 91
 REFERENCES . . . . .	 99

LIST OF TABLES

Table		Page
1.1	Mileage of Concrete Pavements . . . . .	2
2.1	Calculated Surface Temperatures for Different Situations . . . . .	17
3.1	Correlation Factors for Thermistor Temperature Adjustment . . . . .	35
3.2	Scanner Channel Numbers and Thermistor Locations . . . . .	36
4.1	Thermistor Scan Schedule . . . . .	48
5.1	Percentage of Time that Temperature Differentials can be Detected . . . . .	83

This page replaces an intentionally blank page in the original.

-- CTR Library Digitization Team

## LIST OF FIGURES

Figure		Page
1.1	IRT Results of Preliminary Experiment on November 26, 1979 . . . . .	5
2.1	The Thermal Systems . . . . .	10
2.2	Conductance of Air Spaces Calculated from Experimental Data . . . . .	14
2.3	Average Annual Components of Radiation Balance for the System Space-Atmosphere-Earth (BTU/sq ft) . . . . .	19
3.1	Site Location at Balcones Research Center . .	26
3.2	Slab Dimensions and Void Locations . . . . .	28
3.3	Thermistor Locations . . . . .	30
3.4	Schematic Diagram of Temperature Monitoring System . . . . .	32
3.5	Variance of Thermistor Readings versus Actual Temperature . . . . .	34
3.6	Cross section of a Void . . . . .	39
3.7	Typical Void Design . . . . .	40
3.8	Truck Mount for Infrared Scanner . . . . .	44
4.1	Typical Scatter of Surface Temperatures . . .	51
4.2	Temperatures of the Void System (Stations B, C, H) . . . . .	53
4.3	Temperatures of the Solid System (Stations A, E, J) . . . . .	54
4.4	Temperatures of the Void System (B, C, H) . .	55
4.5	Temperatures of the Solid System (A, E, J) . .	56
4.6	Temperatures of the Void System (B, C, H) . .	57
4.7	Temperatures of the Solid System (A, E, J) . .	58
4.8	Temperatures of the Void System (B, C, H) . .	60
4.9	Temperatures of the Solid System (A, E, J) . .	61
4.10	Temperatures of the Void System (B, C, H) . .	62
4.11	Temperatures of the Solid System (A, E, J) . .	63
4.12	IRT Scan - 6:30 AM . . . . .	65
4.13	IRT Scan - 9:02 AM . . . . .	66
4.14	IRT Scan - 10:05 AM . . . . .	67
5.1	Values of $\Delta T = T_{\text{void}} - T_{\text{solid}}$ at Levels 3, 4, and 9 . . . . .	71
5.2	Values of $\Delta T = T_{\text{void}} - T_{\text{solid}}$ at Levels 3, 4, and 9 . . . . .	72
5.3	Values for $\Delta T = T_{\text{void}} - T_{\text{solid}}$ at Levels 3, 4, and 9 . . . . .	73

FIGURE		Page
5.4	Values for $\Delta T = T_{\text{void}} - T_{\text{solid}}$ at Levels 3, 4, and 9 . . . . .	74
5.5	Values for $\Delta T = T_{\text{void}} - T_{\text{solid}}$ at Levels 3, 4, and 9 . . . . .	75
5.6	Average Surface Temperature Differentials . .	79

## CHAPTER 1. INTRODUCTION

### 1.1 Nature of the Problem

One of the primary factors that cause local failures in reinforced concrete pavements (RCP) is nonuniform foundation support due to the presence of voids at the pavement/subbase interface. Recent work by Birkhoff and McCullough has verified the existence of these voids and provided an insight into their damaging effect on the pavement structure (2).

The design of pavements assumes uniform foundation support from the soil below. When a void develops, that assumption is no longer valid. As a result, stress levels in the pavement rise. An 18-square-foot (1.67-square-meter) void will increase stress levels by 12 percent and a 70-square-foot (6.50-square-meter) void will produce a 56 percent increase under a standard load (2). Over a period of time these higher levels of stress will cause fatigue failures in the pavement structure.

Three major mechanisms for the generation of voids can be identified (2).

- 1) pumping of the subbase material,
- 2) shrinking or swelling of the foundation soils due to a change in moisture content, and
- 3) nonuniform additional densification of the subbase and foundation soils.

The amount of differential movement needed to remove support from a pavement section can be as little as 0.050 in. (1.3 mm) (2). This gap will allow sufficient deflection in the pavement to significantly increase stress levels and lower the fatigue life of the pavement structure.

To help appreciate the problem of voids, the mileage of concrete pavement in Texas and the United States is shown below in Table 1.1.

TABLE 1.1 Mileage of Concrete Pavements (10)

System	Texas (lane-miles)	U.S.
Local Roads		
Rural	2,263	56,279
Municipal	6,151	58,689
State Highways	6,870	142,099
Federal Highways	8,255	123,511
TOTAL	23,539	380,578

Note: 1 mile = 1.6 kilometer

The portion of these roads which is subject to void creation can only be estimated. However, with so many rigid concrete pavements in use and the ever-increasing costs of

maintenance, the problem of voids under pavements cannot be ignored. For example, about 22 percent of the state of Texas, including Dallas-Fort Worth, Houston, San Antonio, and Austin, is underlain by clays susceptible to swelling (11). This fact provides an idea of the magnitude of the problem in Texas. Insufficient data exist to say what the magnitude of the problem is nationally. However, whatever the extent of the problem, it merits immediate attention and research to help lower the costs of highway maintenance and to provide a better service to the public.

The foremost problem in the treatment of voids is their detection. If voids could be located prior to pavement failure, they could be filled by injection with cement grouts, polymers or similar materials. This would return the pavements to full design strengths and preclude early failures. Various mechanical means for detecting voids have been studied, including deflection measurements, vibration, and pumping ( 2 ). These methods, though showing some promise, are time-consuming and results are often hard to precisely analyze. Detection techniques are needed which are simple to use and which offer rapid and reliable results.

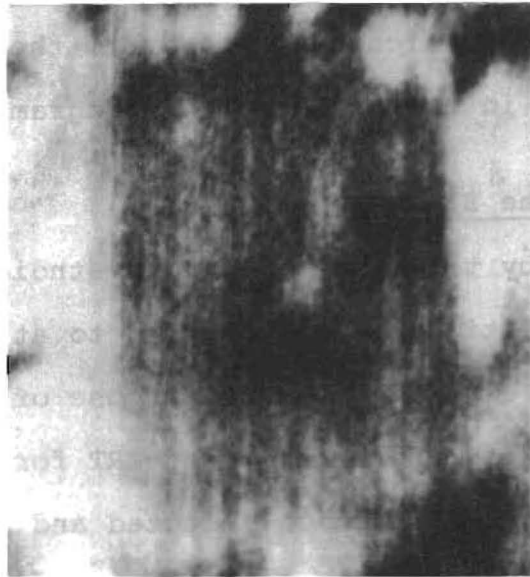
## 1.2 Previous Studies in Infrared Detection of Voids

In August, 1978, at the 4th Biennial Infrared Information Exchange, Holt and Manning presented a paper which

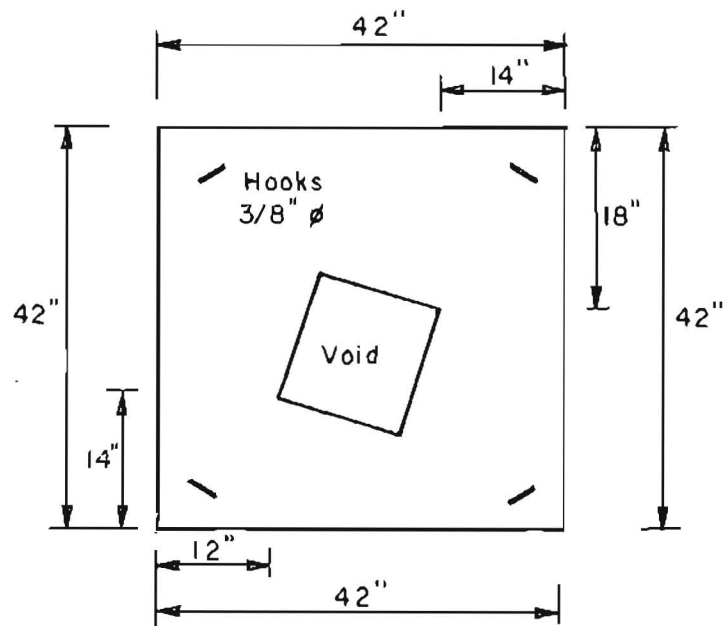
demonstrated infrared thermography (IRT) to be capable of detecting shallow voids 2 inches (5.1 cm) below the pavement surface caused by delaminations in concrete bridge decks due to corrosion of the reinforcing steel. IRT produced an image of the surface temperature differential of the bridge deck. It was found that areas with voids had significantly different surface temperatures than areas of solid concrete (5).

In November, 1979, a preliminary study was conducted at Balcones Research Center at The University of Texas at Austin to determine whether or not a void could be detected through 8 inches of concrete using IRT. A small pad, 3 1/2 ft x 3 1/2 ft x 8 in. (107 cm x 107 cm x 20.3 cm), was cast-in-place above a void measuring 15 in x 15 in x 3 in (38.1 cm x 38.1 cm x 7.6 cm) thick that was protected by falsework, which was later removed. Using a Bendix LN-2 Thermal Mapper (see Appendix 1) mounted on a moving truck, a distinct image showing a clear temperature differential that exactly corresponded to the location of the void was obtained (3).

Figure 1.1a shows the thermal image of the pad produced at 11:15 on November 26, 1979. The air temperature was 63°F (17.3°C); there was a relative humidity of 35% under sunny/clear skies and a light breeze from the SE at 5-10 mph. The ground speed of the truck was 4 ft/sec



(a) Thermal Image



(b) Pad Dimensions - As Built

FIGURE 1.1. IRT Results of Preliminary Experiment on November 26, 1979.

(1.2 m/sec). This image shows a distinct dark area (cooler surface temperature) which corresponds to the location of the void as shown in the accompanying diagram.

### 1.3 Purpose of the Study

Prompted by the success of both studies mentioned in the previous section, it was decided to attempt a more exact, controlled experiment. The purpose of this experiment was to verify the feasibility of IRT for the detection of voids. The course of action selected and the results of the experiment are described in this report. The experiment was strictly of a preliminary nature, designed to see if voids could be detected under realistic conditions. An effort was also made to monitor the effect of voids on the temperature regimens observed in the slab-soil system. This provided valuable background data necessary to explain the applicable heat transfer mechanisms involved in surface temperature differentials.

### 1.4 Scope of the Study

The scope of the study is as follows:

- 1) A theoretical analysis of the thermal properties of a slab/soil system and a slab/void/soil system has been made to predict the effect of the void on surface temperatures.
- 2) A full-scale model of a pavement slab has been cast-in-place above thin voids. Temperature data were collected in both the concrete and the underlying soils.

- 3) Comparisons were made between temperatures measured in the areas with voids and those in areas without voids.
- 4) A single IRT scan with state-of-the-art equipment was performed to see if the voids could be detected by the observed surface temperature differentials.

### 1.5 Organization of the Report

Chapter 2 deals with the applicable theories involved in the heat transfer in the slab/soil and slab/void/soil systems. Sample calculations are made to predict the effect of the void on surface temperatures.

Chapter 3 outlines the design and construction of the experimental pavement slab and its temperature monitoring system. The infrared equipment used in the study is also described.

Chapter 4 graphically presents the temperature data collected and the results of the IRT scan.

Chapter 5 presents the analysis of the experiment. Comparisons are made between the two thermal systems. The observed data are, in turn, compared with the predictions evolved in Chapter 2.

Chapter 6 outlines the conclusions and future recommendations for further experiments in this field.

This page replaces an intentionally blank page in the original.

-- CTR Library Digitization Team

## CHAPTER 2. THEORETICAL ANALYSIS

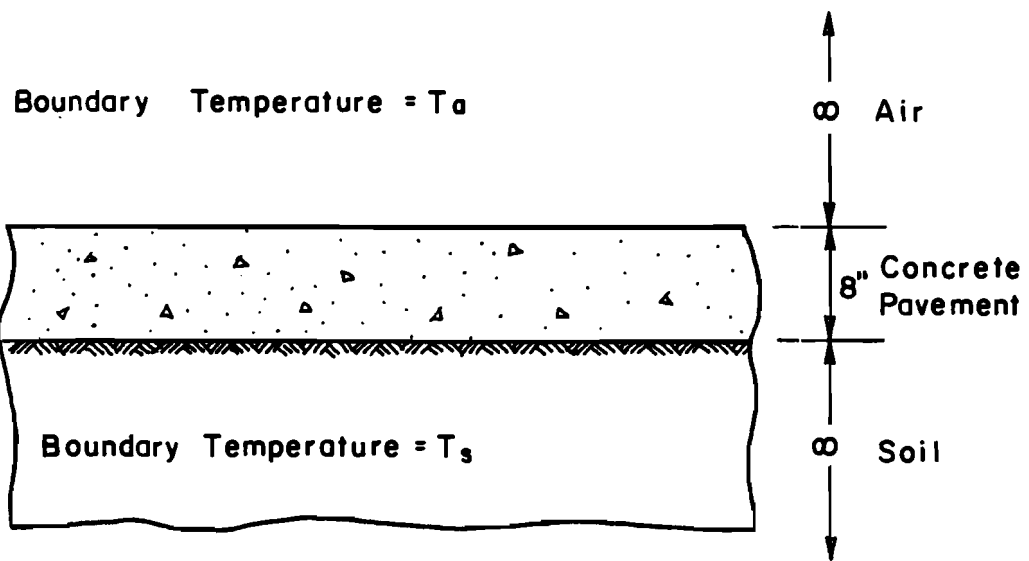
In keeping with the preliminary nature of this study, the theoretical analysis discussed in this chapter considers pavement systems under ideal conditions.

It is not within the scope of this report to address all of the parameters that eventually will have to be studied in relation to the detection of voids with infrared thermography. Indeed, one of the primary concerns of this study has been the identification of the relative parameters that will have to be considered before this method can be put to practical use. These parameters will be enumerated in Chapter 6.

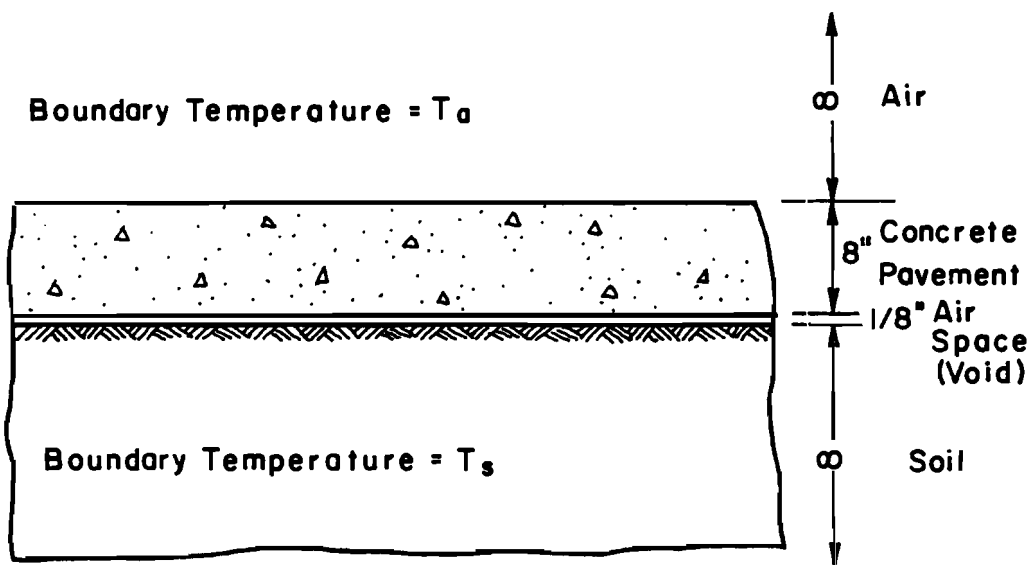
### 2.1 The Pavement Systems

The two pavement systems to be analyzed are shown in Figure 2.1. Figure 2.1(a) portrays a pavement system without a void. The components of this "solid system" are

- 1) an infinite blanket of air above the concrete at a temperature equal to  $T_a$ ,
- 2) 8 inches of plain concrete, and
- 3) an infinite body of homogeneous soil below the concrete at a temperature equal to  $T_s$ .



(a) Solid System



(b) Void System

Figure 2.1. The Thermal Systems.

Figure 2.1(b) is identical to 2.1(a) with the addition of a void 1/8 in. (3.2 mm) thick at the soil/concrete interface. One-eighth inch is chosen because it is the thinnest air space for which thermal conductivity measurements have been done, and because it is a realistic thickness for voids under pavements. Eight inches of concrete is used because many concrete pavements in Texas are of this thickness.

## 2.2 Thermal Model

The source of all the heat in the two systems is solar radiation. This analysis will not consider the effect of this radiation directly, but will consider air temperatures adjusted to account for the effect of the radiation.

The air temperature rises and falls in direct relation with the amount of radiation passing through it. This radiant energy is converted into heat as it hits and penetrates the surface of the concrete. The net effect, then, of radiation on the concrete surface is one of an elevated air temperature. For example, experimental results have shown that, if the air temperature on a bright, sunny afternoon is 95°F (35°C), the concrete surface temperature will be around 125°F (57.2°C), due to the radiant energy from the sun. The same situation would occur if the air temperature was elevated to about 135°F (57.2°C) and no

radiation was allowed to hit the surface. This simplification of the actual situation makes a heat transfer analysis of the pavement systems possible.

2.2.1 Parameters and Symbols. The basic equation for the calculation of temperatures at any point within a system under steady-state conditions is

$$T_x = T_1 - \frac{R_1}{R_t} (T_1 - T_2) \quad (1)$$

where  $T_x$  = temperature at any point in the system  
 $T_1$  = temperature at one boundary of the system  
 $T_2$  = temperature at the other boundary  
 $R_t$  = total thermal resistance of the system  
 $R_1$  = the thermal resistance measured from the first boundary to any point within the system.

In the particular case of the two pavement systems,

$T_x$  = surface temperature  
 $T_1 = T_s$  = soil temperature  
 $T_2 = T_a$  = air temperature  
 $R_t$  = total resistance of each system  
 $R_1$  = the thermal resistance measured from the bottom of each system to the surface, but not including the surface resistance of the concrete.

The symbols and units to be used in this analysis are

$U$  = overall coefficient of heat transmission of a system (BTU/hour-sq ft-  $\Delta^\circ\text{F}$ ) (Cal/day-sq cm-  $\Delta^\circ\text{C}$ )

$k$  = thermal conductivity of a homogeneous material  
(BTU/hour-sq.ft- $\Delta$  °F/inch of thickness of  
material) (Cal/day-sq cm- $\Delta$  °C)

$t$  = thickness of the material (inch) (cm)

$C = \frac{k}{t}$  = thermal conductance between two surfaces

$f$  = surface conductance at an air-surface inter-  
face by radiation and convection (BTU/hour-  
sq ft-°F)

$\Delta T$  = temperature difference between the boundaries  
(F° or C°)

$a$  = thermal conductance of an air space, including  
convection, radiation, and surface conductances  
(BTU/hour-sq ft-°F)

$R$  = thermal resistance, obtained from the recipro-  
cal of the heat transfer as expressed by  $U$ ,  
 $C$ ,  $f$ , or  $a$  (°F-sq.ft-hour/BTU) (°C-sq cm-day/  
Cal)

Particular values for the elements of the two  
systems are

$k_{\text{concrete}} = k_c = 12.1 \text{ BTU/hr-sq ft-} \frac{\text{°F}}{\text{inch}} \text{ thickness}$

$C_{8\text{-in. concrete}} = \frac{k_c}{t_c} = 12.1/8 = 1.51 \text{ BTU/hr-}$   
 $\text{sq ft-} \frac{\text{°F}}{\text{°F}}$

$f_{\text{concrete surface}} = 1.63 \text{ BTU/hour-sq ft-} \frac{\text{°F}}{\text{°F}}$  for  
upward heat flow, and  
 $= 1.08$  for downward heat flow (1)

$a$  = thermal conductance for a 1/8-in. air space,  
which varies as shown in Figure 2.2

(Note: 1.0 BTU/hour-sq ft = 0.153 Cal/day-sq cm)

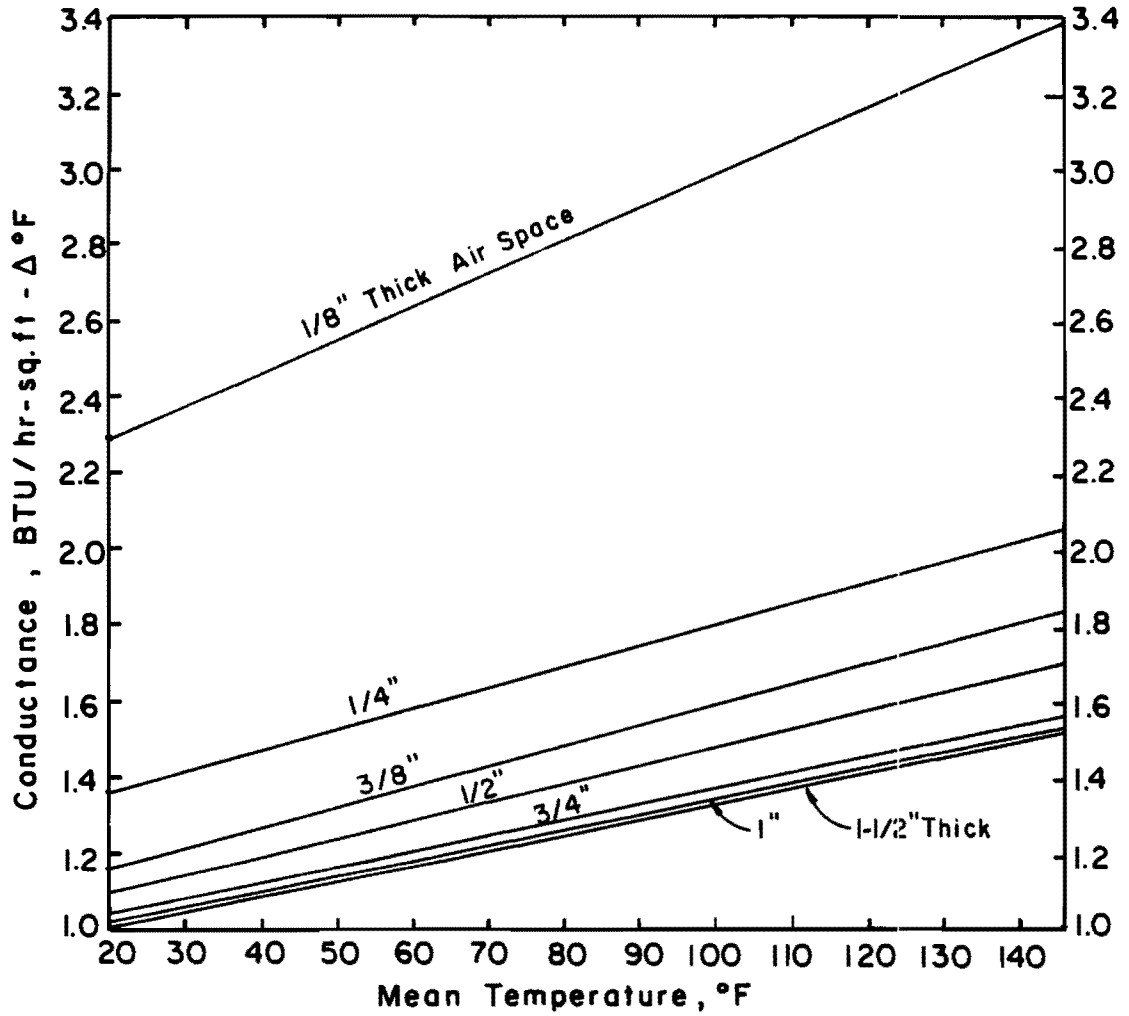


Figure 2.2. Conductance of Air Spaces Calculated from Experimental Data (7)

2.2.2 Calculations of Surface Temperatures. Surface temperatures are calculated for five different situations typical to the Central Texas area:

- 1) A summer afternoon with  $T_a = 125^\circ\text{F}$  ( $51.7^\circ\text{C}$ ), adjusted for radiation, and  $T_s = 90^\circ\text{F}$  ( $32.2^\circ\text{C}$ ),
- 2) A summer night with  $T_a = 70^\circ\text{F}$  ( $21.1^\circ\text{C}$ ) and  $T_s = 85^\circ\text{F}$  ( $29.4^\circ\text{C}$ ).
- 3) A winter afternoon with  $T_a = 70^\circ\text{F}$  ( $21.1^\circ\text{C}$ ), adjusted for radiation, and  $T_s = 50^\circ\text{F}$  ( $10^\circ\text{C}$ ).
- 4) A winter night with  $T_a = 30^\circ\text{F}$  ( $-1.1^\circ\text{C}$ ) and  $T_s = 45^\circ\text{F}$  ( $7.2^\circ\text{C}$ ).
- 5) A situation when  $T_a = T_s$ .

Case 1 - A Summer Afternoon (heat flow down):

Solid System

$$F_t = \frac{1}{f_c} + \frac{1}{C_c} = \frac{1}{1.08} + \frac{1}{1.51} = 1.59 \quad \text{°F-sq ft-hour/BTU}$$

$$R_1 = \frac{1}{C_c} = \frac{1}{1.51} = 0.66$$

therefore,

$$T_{x_{\text{solid}}} = T_s - \frac{R_1}{R_t} (T_s - T_a) = 104.5^\circ\text{F} \quad (40.3^\circ\text{C})$$

Void System

$$R_t = \frac{1}{f_c} + \frac{1}{C_c} + \frac{1}{a} \quad \text{where } a = 2.95 \text{ at } 90^\circ\text{F} \text{ (see Figure 2.2)}$$

$$R_t = \frac{1}{1.08} + \frac{1}{1.51} + \frac{1}{2.95} = 1.93 \quad \text{°F-sq ft-hr/BTU}$$

$$R_1 = \frac{1}{C_c} + \frac{1}{a} = \frac{1}{1.51} + \frac{1}{2.95} = 1.00$$

therefore,

$$T_{x_{\text{void}}} = 108.1^{\circ}\text{F} \quad (42.3^{\circ}\text{C})$$

$$\Delta T = T_{x_{\text{void}}} - T_{x_{\text{solid}}} = 3.6^{\circ}\text{F} \quad (2.0^{\circ}\text{C})$$

Table 2.1 shows the results of calculations for Case 1 as well as from similar calculations for the other four cases mentioned above.

As can be seen from the results shown in Table 2.1, the surface temperature above a void will be warmer than the surrounding concrete when the steady-state air temperature is greater than the steady-state soil temperature. Conversely, the surface above a void will be cooler when the steady-state air temperature is less than the steady-state soil temperature. When the soil and air temperatures are the same, the surface temperatures will be uniform.

Under actual conditions, these steady-state conditions do not exist. The steady-state calculations assist, however, in visualizing trends for a certain cycle of air and soil temperatures. Air temperatures over a certain period of time will exhibit cyclic characteristics, between high temperatures in the afternoon and low temperatures at night. Likewise, soil temperatures exhibit the same cyclical pattern, but with much less difference between the peaks and valleys. Both soil and air temperatures vary according to the amount of radiation

TABLE 2.1 Calculated Surface Temperatures  
for Different Situations

Situation	$T_s$ °F (°C)	$T_a$ °F (°C)	$T_{xv}$ °F (°C)	$T_{xs}$ °F (°C)	$T=T_{xv}-T_{xs}$ °F (°C)
1. Summer Afternoon (Heat flow down)	90 (32.2)	125* (51.7)	108.1 (42.3)	104.5 (40.3)	+3.6 (+2.0)
2. Summer Night (Heat flow up)	85 (29.4)	70 (21.1)	75.6 (24.2)	77.3 (25.2)	-1.7 (-0.9)
3. Winter Afternoon (Heat flow down)	50 (10.0)	70* (21.1)	60.6 (15.9)	58.3 (14.6)	+2.3 (+1.3)
4. Winter Night (Heat flow up)	45 (7.2)	30 (-1.1)	35.6 (2.0)	37.3 (2.9)	-1.7 (-0.9)
5. Air Temp. = Soil Temp.	75 (23.9)	75 (23.9)	75 (23.9)	75 (23.9)	-0-

\* Adjusted for effects of solar radiation

$T_s$  = temperature of the soil

$T_a$  = temperature of the air

$T_{xv}$  = surface temperature above the void system

$T_{xs}$  = surface temperature above the solid system

that they absorb or emit over a period of time. The dynamic aspects of the surface temperature variations can, therefore, be better visualized by examining the "radiation balance" within the two systems.

### 2.3 Radiation Balance Model

The "radiation balance" or "energy balance" concept has been developed as a means of analyzing the total radiation flux at the surface of the earth. The basic equation for this concept is

$$H = S(1.0-r) - S_b \quad (6)$$

where  $H$  = net radiation received by a horizontal surface at the earth

$S$  = the solar radiation reaching that surface

$r$  = the reflection coefficient of that surface

$S_b$  = effective terrestrial radiation emitted by the surface

Figure 2.3 shows the average annual components of the radiation balance for the space-atmosphere-earth system. The law of the conservation of energy holds true in all aspects of this diagram. Incoming solar radiation is equal to  $97 \times 10^4$  BTU/sq ft (263 kcal/sq cm). Outgoing reflected solar radiation,  $38 \times 10^4$  BTU/sq ft (1.03 kcal/sq.cm), and outgoing long-wave-terrestrial radiation,  $59 \times 10^4$  BTU/sq ft (163 kcal/sq.cm), sum up to the total incoming solar radiation. Likewise, at the earth's surface, the emitted radiation is equal to the absorbed radiation.

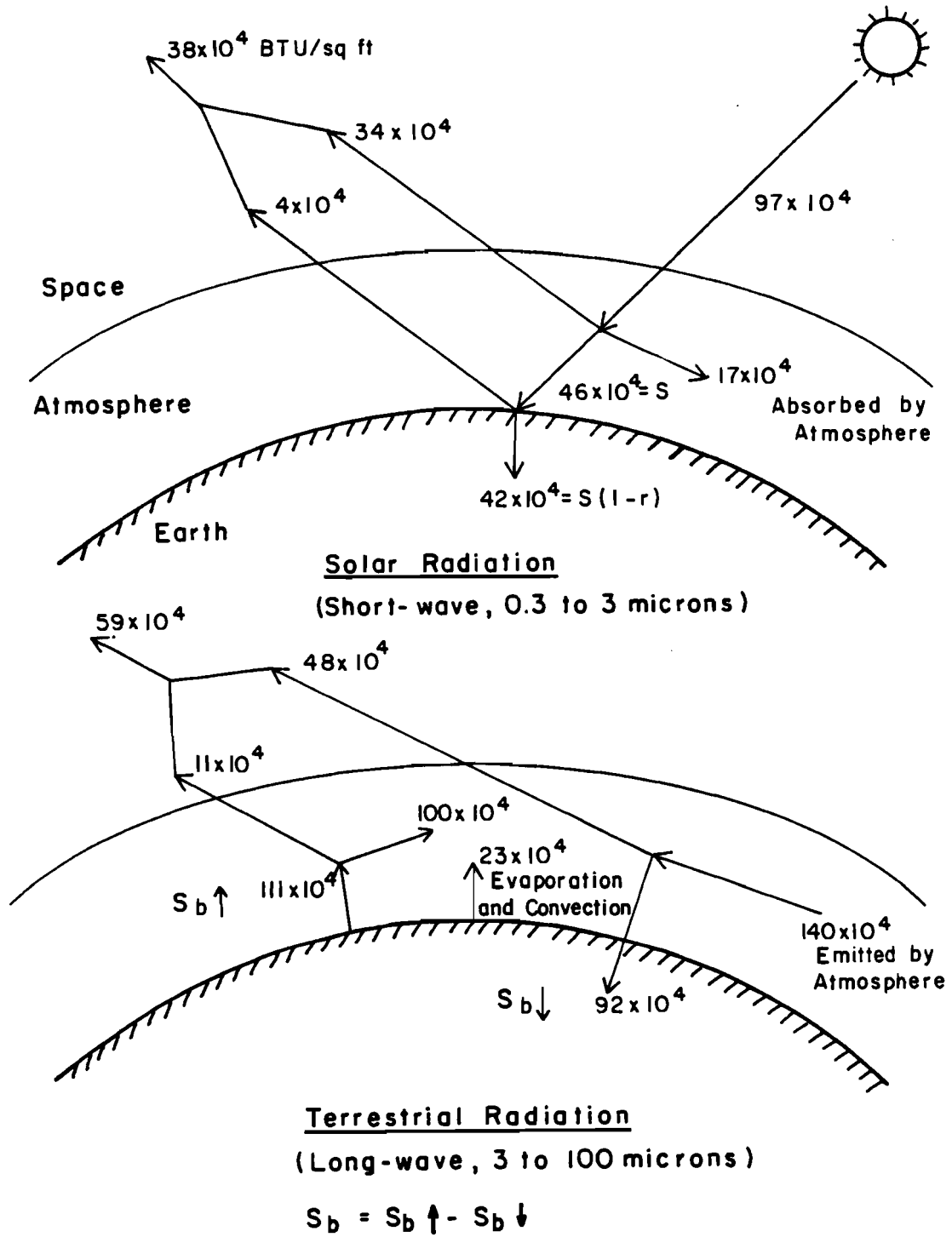


Figure 2.3. Average Annual Component of Radiation Balance for the System Space-Atmosphere-Earth. (BTU/sq ft) (6)

The inherent balance described in Figure 2.3 would seem to indicate that the detectable radiation from a homogeneous surface will always be constant. Over a long period of time, that is true, as shown by the summation of the annual components of solar, short-wave radiation and terrestrial, long-wave radiation. However, momentary imbalances in the terrestrial radiation can be expected. These imbalances over a homogeneous surface are directly related to the different thermal resistances exhibited by different areas of the body.

The model of the homogeneous concrete slab with intermittent voids at the subbase/slab interface affords such an example. During the course of the day, month, or year, the net long-wave radiation emitted from all areas of the slab will be equal. Also, at all times, each square foot of the slab receives the same amount of atmospheric and solar radiation. What is different is the manner in which that incoming radiation is stored as heat in the two different systems on an hourly basis and how it is eventually emitted back into the atmosphere as long-wave radiation on an hourly basis.

The higher resistance of the voided system will store more of the radiant heat energy in the concrete, whereas the solid concrete system will transmit more heat down into the soil, due to its overall lower resistance

to heat transfer. Therefore, it can be concluded that during the day, when solar radiation levels are highest, the concrete above the void will have more absorbed energy and a correspondingly higher temperature. In the solid system more heat energy will have been transferred into the soil below, yielding less stored energy in the concrete.

At night, the systems are no longer absorbing radiation from the sun. Both systems begin to emit the stored energy from the previous day. But the void system has stored more energy closer to the surface and, therefore, will give up its energy to the atmosphere more quickly than the solid area, which has stored the energy deeper. As a result of the continued higher levels of radiation from the solid areas of the slab, the temperatures can be expected to be cooler above a void. The net energy absorbed and emitted by both systems will be the same for the day in question but the hourly levels of radiation for the two systems will be different.

#### 2.4 Detection of Infrared Radiation

The human eye is sensitive to only a very narrow range of the electro-magnetic spectrum, between 0.45 microns and 0.75 microns. Beyond this range is the infrared region of the spectrum, which is followed by the microwave region. The infrared zone is considered to be between 0.75 microns and

1000 microns. This can be further subdivided into three regions, "near" (0.75 to 1.50 microns), "intermediate" (1.50 to 10.0 microns), and "far" (beyond 10 microns)( 8 ). The region beyond 300 microns is often referred to as the "submillimeter" region, since the division between the infrared zone and the microwave region is not easily defined.

The amount of electromagnetic radiation emitted by an object is dependent upon the temperature of the body as well as its surface emissivity. The emissivity is a measure of the percentage of radiation that is absorbed by the body, as opposed to the amount reflected by the surface. The sum of the emissivity and the reflectivity of a given body must always be equal to one, so that there is no net loss of energy in the system.

Since the amount of radiation emitted by a surface is also directly related to the surface temperature, measurements of the infrared radiation emitted by a given surface can provide an indirect measure of the surface temperature. Provided that the emissivity of the surface is constant, small variations in surface temperatures of a body will form a thermal image that can be related to the different thermal resistances in different parts of the body.

Most modern infrared detectors focus on infrared radiation in the 8 to 14 micron (intermediate and far)

range ( 8 ). This range is generally considered to be the most constant within the infrared spectrum and, therefore, the most reliable.

A significant portion of the terrestrial, long-wave radiation (3 to 100 microns) emitted from the surface of the earth will be detected within the 8 to 14 micron range. All other wavelengths can be filtered out to avoid background noise. Precise readings in this range have been shown to correlate closely with the temperature pattern of a surface (8)

If the emissivity of concrete is considered to be constant and all other factors in the two systems discussed in this chapter are constant (composition and thickness), a thermal image of a pavement with some voided areas would show surface temperature differentials which correspond to the location of the voids, i.e., areas of greater thermal resistance. Therefore, voided areas of a concrete pavement should be easily discernible in an infrared thermal image of the surface.

Chapter 3 presents the experimental set-up and methodology used in an effort to substantiate this hypothesis.

This page replaces an intentionally blank page in the original.

-- CTR Library Digitization Team

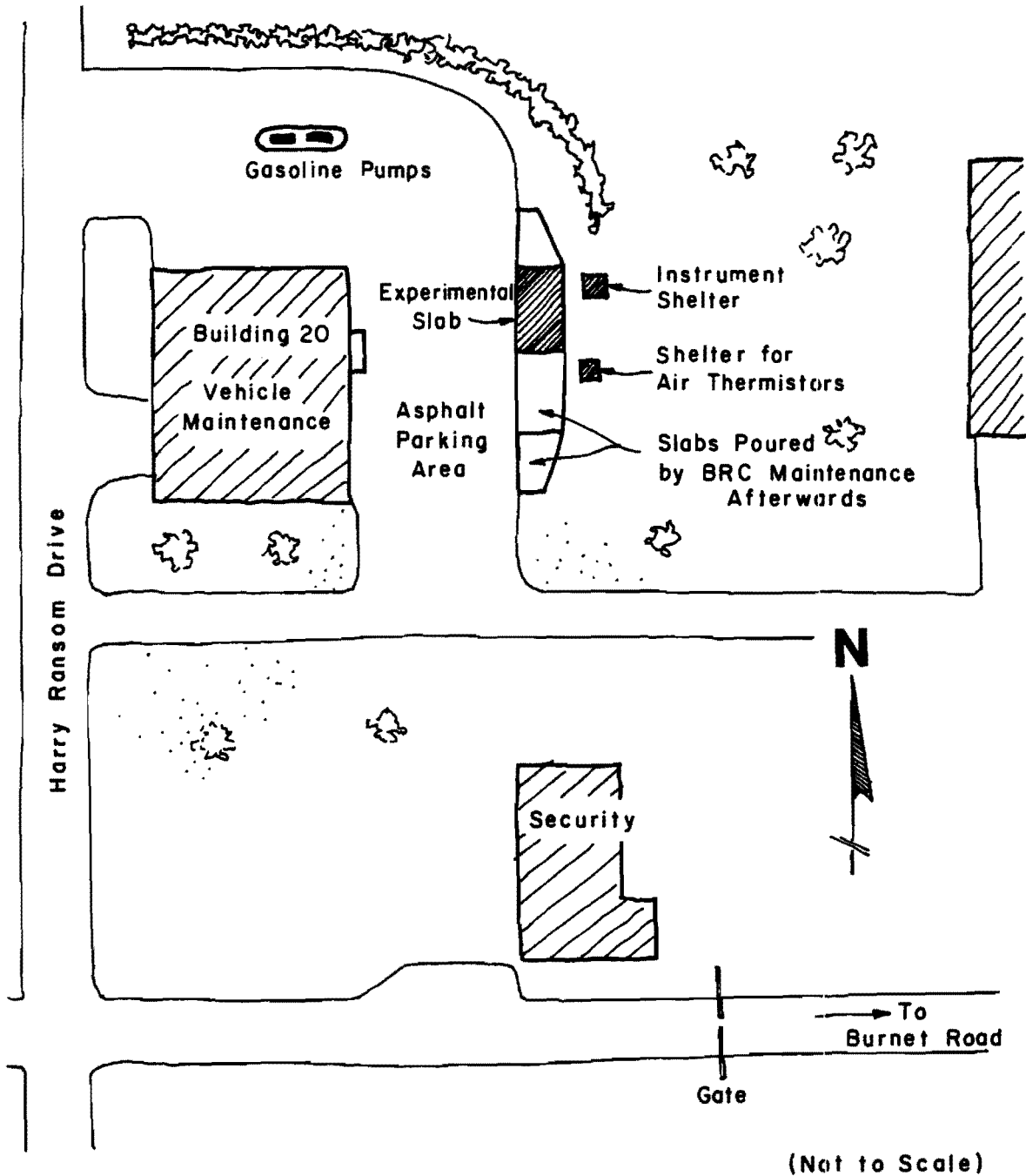
## CHAPTER 3. DESCRIPTION OF EXPERIMENT

Based upon the favorable results in previous experiments described in Chapter 1, a more detailed experiment was designed. A large slab was placed with several large voids at the subbase/slab interface. Sensitive temperature recording devices were used to monitor temperatures in the air, concrete, voids, soil beneath the slab, and soil away from the slab. Temperatures were taken at various levels where voids occurred as well as in the solid system areas.

The site of the experiment is behind Building #20, adjacent to the parking lot at Balcones Research Center of UT Austin. Additional slabs have since been placed longitudinally on both sides of the experimental slab to provide additional parking for BRC personnel. Figure 3.1 shows the site diagram.

### 3.1 General Slab Dimensions

The as-built dimensions for the experimental slab are 12 ft x 21 ft x 8 in. (3.66 M x 6.40 M x 20 cm). The width of 12 ft was used to model a standard lane-width



(Not to Scale)

Figure 3.1. Site Location at Balcones Research Center

used in highway constructions. Likewise, the 8-in. pavement thickness was used to provide a realistic situation. The 21 ft of length provides sufficient room for three large voids.

Slab dimensions and void locations are shown in Figure 3.2. Void No. 1, 3 ft x 5 ft (91 cm x 152 cm), is located widthwise in the center of the slab, therefore minimizing edge effects. Void No. 2, 2 ft x 4 ft (61 cm x 122 cm), is placed at the pavement edge since it is thought that many voids tend to originate at that point. Void No. 3, 3 ft x 3 ft (91 cm x 91 cm), was included as a check for Void No. 1.

The slab was reinforced according to a typical highway design. Transverse reinforcing was #3 bars (9.5 mm) at 18 inches (46 cm) on-center. Longitudinal reinforcing was #3 bars at 12 inches (30 mm) on-center. The steel is centered at mid-depth in the slab. Due to the small percentage of steel in the slab and its high thermal conductivity, it can be shown that the steel has no effect on the overall thermal conductivity of the slab.

### 3.2 Temperature Monitoring System

3.2.1 Equipment. The small variations in temperatures predicted in Chapter 2 dictated that the temperature measuring system be capable of measuring to an accuracy of

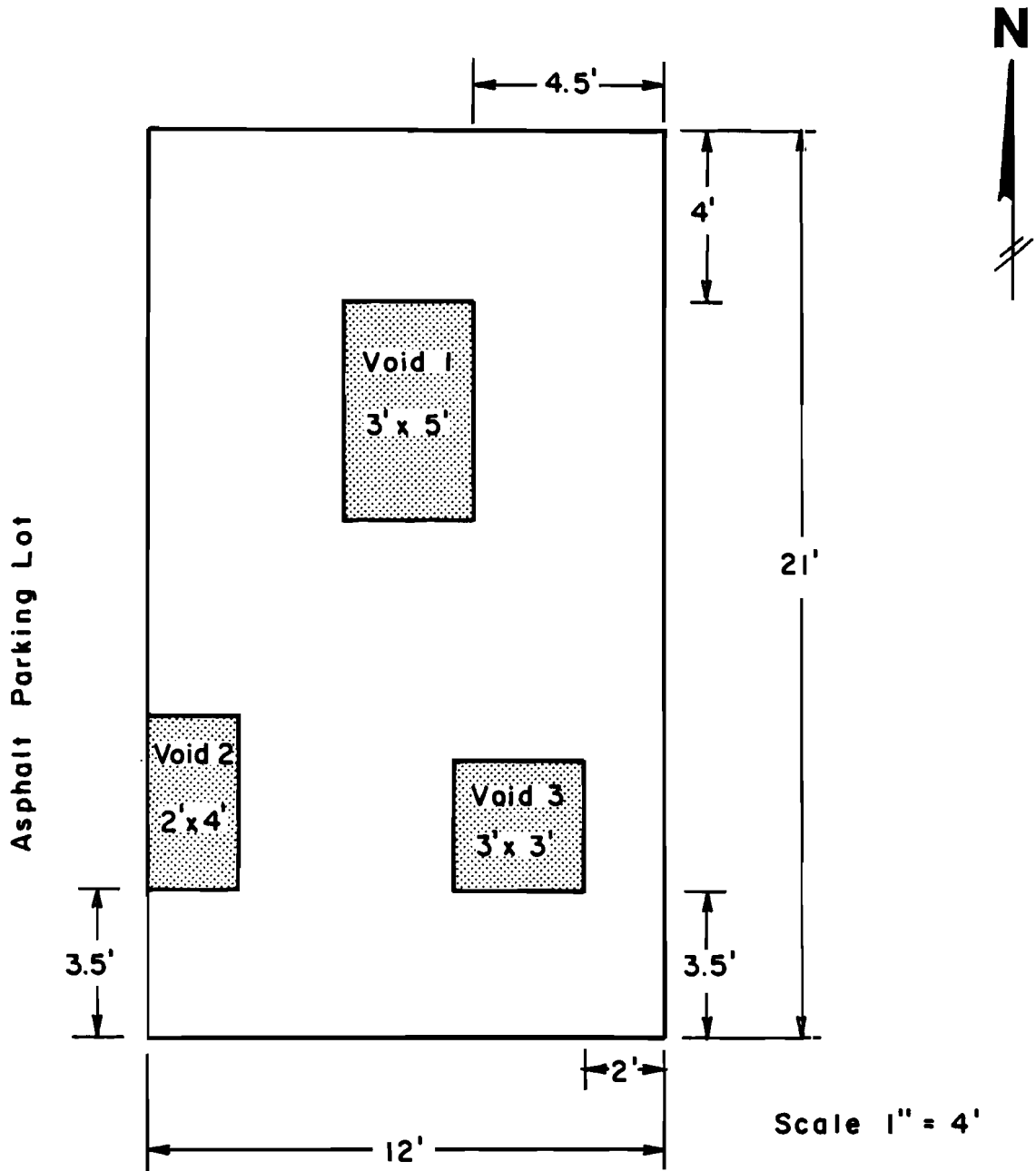
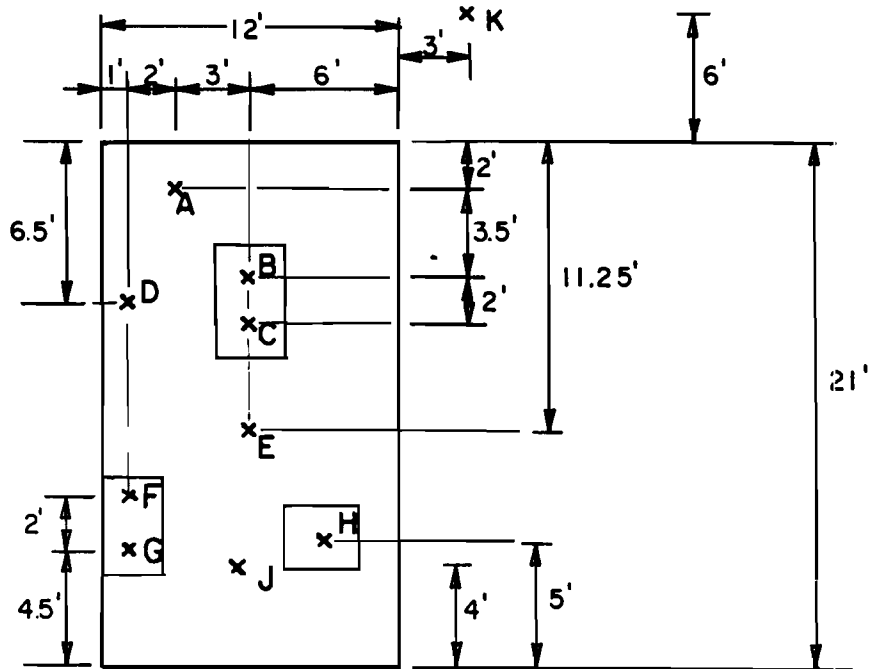


Figure 3.2. Slab Dimensions and Void Locations

around  $\pm 0.1$  to  $0.2^{\circ}\text{F}$  ( $0.06$  to  $0.11^{\circ}\text{C}$ ). Since many separate readings had to be made on a periodic basis, the equipment had to have a large capacity and automatic functioning mode set on a predetermined time period. Fortunately, a system meeting these requirements had been designed previously for use in other research at the University (9). The system consists of these major parts:

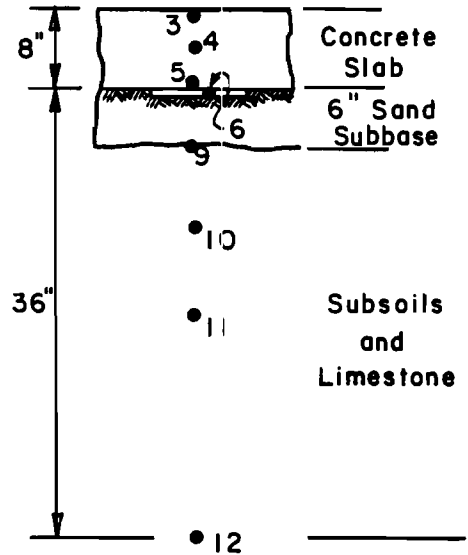
- 1) 67 highly accurate,  $\pm 0.1^{\circ}\text{F}$  ( $0.06^{\circ}\text{C}$ ), thermistor probes,
- 2) an ARA (Applied Research Austin) SD 100-100 channel electronic scanner,
- 3) ARA ET-200 Digital thermometer,
- 4) ARA printer coupler, and
- 5) a converted Smith-Corona Figurematic adding machine used as the digital printer.

The thermistors, which are essentially heat sensitive resistors, were epoxy covered disk type with a maximum diameter of 0.095 in. (2.4 mm). To prevent water leakage, a liquid RTV (room temperature vulcanizing) silicon rubber was utilized to waterproof each individual thermistor. These thermistors provide near instantaneous reading of temperature with an accuracy of  $\pm 0.1^{\circ}\text{F}$  ( $0.006^{\circ}\text{C}$ ). Sixty-seven thermistors were used in the experiment. Their locations and depths are shown in Figure 3.3. In addition to the 65 soil and concrete thermistors, two thermistors were placed in a standard environmental instrument box to monitor air temperature.



Thermistor Stations A-K

Station	3	4	5	6	8	9	10	11	12
	Concrete Surface	Mid-depth Concrete	Bottom of Concrete	Void	3" Below Surf.	6" Below Slab	12" Below Slab	18" Below Slab	36" Below Slab
A	x*	x	x			x	x	x	x
B	x	x	x	x		x	x	x	x
C	x	x	x	x					
D	x	x	x			x	x	x	x
E	x	x	x			x	x	x	x
F	x	x	x	x		x	x	x	x
G	x	x	x	x					
H	x	x	x	x		x	x	x	x
J	x	x	x			x	x	x	x
K					x	x†	x†	x†	x†



\* x = Indicates a Thermistor at that Station and Level  
 † = Depth is Below Soil Surface

Thermistor Levels

Figure 3.3. Thermistor Locations

Figure 3.4 presents a schematic diagram of the five major components of the temperature monitoring system. The ARA SD 100 scanner performed the task of automatically sweeping over the array of thermistors and relaying the signal to the digital thermometer. In addition, a binary coded decimal (BCD) electrical output was available to provide the printer with the thermistor number.

The ARA ET 200 digital thermometer converted the input from the thermistors (via the scanner) into a digital reading with a resolution and repeatability of  $\pm 0.1^{\circ}\text{F}$  ( $0.06^{\circ}\text{C}$ ).

The ARA Printer Coupler received the BCD outputs from the scanner and printer and sent the signal to the digital printer. The printer printed first the thermistor number and then its temperature.

A complete scan of the 67 thermistors was done in about two minutes. A timing device was used to trigger the scanner every half-hour to provide periodic data over an extended period of time.

**3.2.2 Calibration.** The system as designed had a close calibration range between  $70\text{-}90^{\circ}\text{F}$  ( $21.1\text{-}32.2^{\circ}\text{C}$ ). This meant the temperature readings would all vary uniformly from a known standard within this range. Outside of this range, the temperature variance was not known. Experimental data were compiled using an accurate mercury thermometer as the standard.

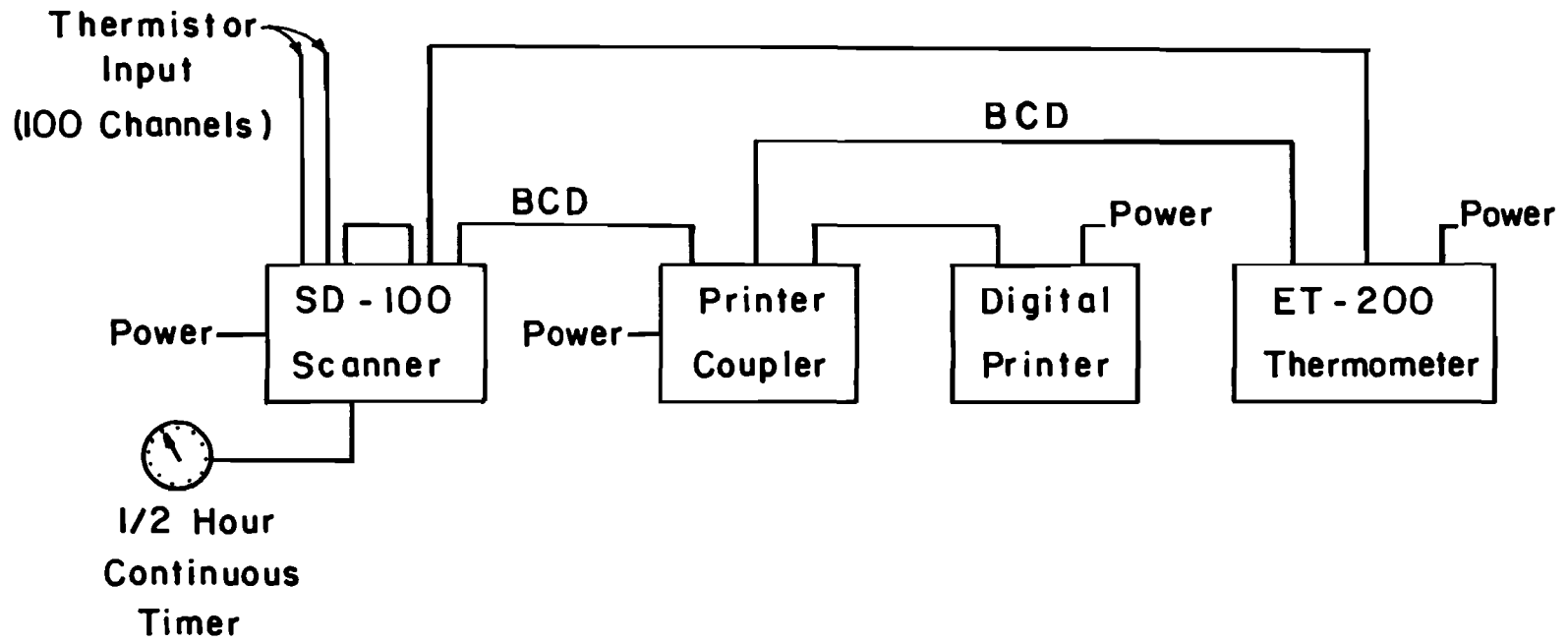


Figure 3.4. Schematic Diagram of Temperature Monitoring System

The 67 thermistors were immersed in water, which provided a uniform, controlled temperature. The temperature of the water, initially at 37.5°F (3.1°C), was increased in 5°F (2.8°C) intervals.

At each interval the thermometer was read, and readings were taken of all the thermistors. Readings were continued up to 130°F. The resulting curve of water temperature (as measured by the standard thermometer) versus temperature variance (as measured by the thermistors) is shown in Figure 3.5. Table 3.1 presents the data from Figure 3.5 in a tabular fashion. Table 3.2 shows the scanner channel and corresponding thermistor station and level.

Using Table 3.1, it is possible to calculate the real temperature from the actual thermistor reading provided by the printer by simply adding the appropriate correction factor.

### 3.3 Void Design

Probably the most formidable problem in the design of this experiment was creating an air space or void beneath a cast-in-place concrete slab with minimum effects on the surroundings. Many ideas were considered and discarded as impractical or infeasible. The final design choice was two sheets of sheet metal separated by intermittent 1/8-inch (3.2-mm) thick plywood strips.

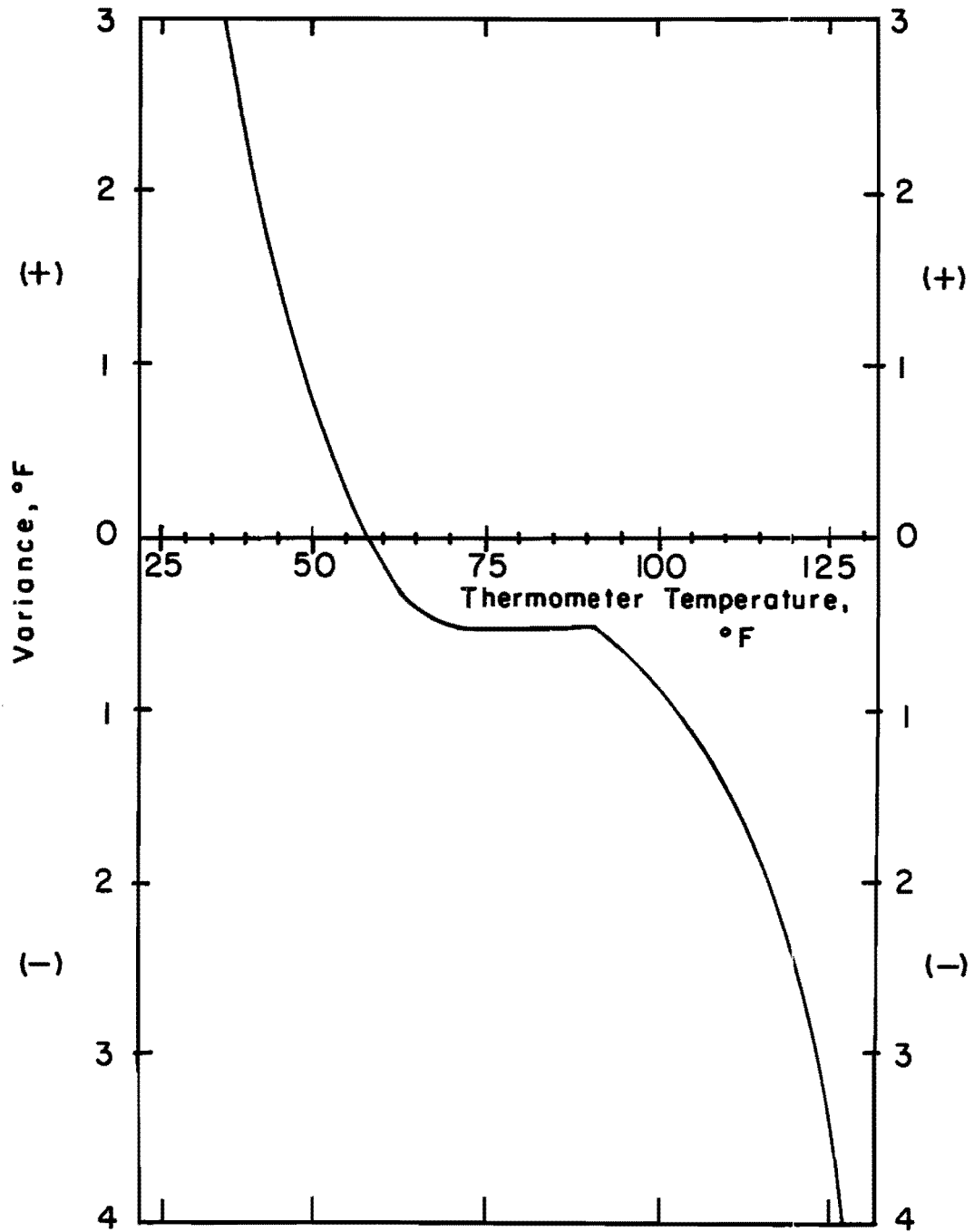


Figure 3.5. Variance of Thermistor Readings versus Actual Temperature

TABLE 3.1 Correction Factors for Thermistor Temperature Adjustment

Temp, °F	Correc- tion, °F	Temp, °F	Correc- tion, °F	Temp, °F	Correc- tion, °F	Temp, °F	Correction, °F
37	-3.0	60	+0.2	83	+0.5	106	+1.2
38	-2.8	61	+0.2	84	+0.5	107	+1.2
39	-2.6	62	+0.3	85	+0.5	108	+1.3
40	-2.4	63	+0.3	86	+0.5	109	+1.4
41	-2.2	64	+0.4	87	+0.5	110	+1.5
42	-2.0	65	+0.4	88	+0.5	111	+1.5
43	-1.8	66	+0.5	89	+0.5	112	+1.6
44	-1.6	67	+0.5	90	+0.5	113	+1.7
45	-1.5	68	+0.5	91	+0.5	114	+1.8
46	-1.4	69	+0.5	92	+0.6	115	+1.9
47	-1.3	70	+0.5	93	+0.6	116	+2.0
48	-1.1	71	+0.5	94	+0.7	117	+2.0
49	-0.9	72	+0.5	95	+0.7	118	+2.2
50	-0.8	73	+0.5	96	+0.7	119	+2.4
51	-0.7	74	+0.5	97	+0.8	120	+2.6
52	-0.6	75	+0.5	98	+0.8	121	+2.8
53	-0.5	76	+0.5	99	+0.8	122	+3.0
54	-0.3	77	+0.5	100	+0.9	123	+3.2
55	-0.2	78	+0.5	101	+0.9	124	+3.4
56	-0.1	79	+0.5	102	+1.0	125	+3.5
57	0.0	80	+0.5	103	+1.0	126	+3.8
58	+0.1	81	+0.5	104	+1.1	127	+4.2
59	+0.1	82	+0.5	105	+1.1	128	+4.5

Note:  $^{\circ}\text{C} = \frac{5}{9} (^{\circ}\text{F} - 32)$  and  $1.0^{\circ}\text{C} = 1.8^{\circ}\text{F}$

TABLE 3.2 Scanner Channel Numbers and  
Thermistor Locations

Scanner Channel	Thermistor Location	Scanner Channel	Thermistor Location	Scanner Channel	Thermistor Location	Scanner Channel	Thermistor Location
0	-	25	H3	50	A9	75	Air 2
1	E3	26	H4	51	A10	76	D9
2	G6	27	H5	52	A11	77	D10
3	G5	28	H6	53	A12	78	D11
4	G4	29	J3	54	F9	79	D12
5	G3	30	J4	55	F10	80	-
6	F6	31	J5	56	F11	81	-
7	F5	32	-	57	F12	82	-
8	F4	33	K8	58	J9	83	-
9	F3	34	K8	59	J10	84	-
10	C6	35	K9	60	J11	85	-
11	C5	36	K10	61	J12	86	-
12	C4	37	K11	62	E9	87	-
13	C3	38	K12	63	E10	88	-
14	B6	39	E5	64	E11	89	-
15	B5	40	-	65	E12	90	-
16	B4	41	-	66	B9	91	-
17	B3	42	-	67	B10	92	-
18	D5	43	-	68	B11	93	-
19	D4	44	-	69	B12	94	-
20	D3	45	-	70	H9	95	-
21	A5	46	-	71	H10	96	-
22	A4	47	-	72	H11	97	-
23	A3	48	-	73	H12	98	-
24	E4	49	-	74	Air 1	99	-

The validity of this model can be appreciated by comparing its overall effects on heat transfer to that of a pure 1/8-inch-thick air space. The two systems to be considered are

- 1) Concrete/Air Space/Soil, and
- 2) Concrete/Sheet Metal/Air Space/Sheet Metal/Soil.

The concrete and soil elements of the two systems are identical. Concrete and soil have thermal conductivity ( $k$ ) values of about 12 BTU/hour-sq ft- $^{\circ}$ F. Steel has a  $k$  value of 312 BTU/hour-sq ft- $^{\circ}$ F. The resistance value for the 8-inches of concrete is 8-in./12 = 0.66 BTU/hour-sq ft- $^{\circ}$ F, whereas the resistance for the sheet metal is  $\frac{0.024\text{-in.}}{312} = 7.7 \times 10^{-5}$  BTU/hour-sq ft- $^{\circ}$ F (for 24 gage sheet metal). (Note: 1.0 BTU/hour-sq ft = 0.153 Cal/day-sq cm)

Such a low comparative resistance will yield no noticeable net effect on the system. The only other mode of heat transfer to be considered is that by radiation in the air space. Heat transfer by radiation in an air space is directly related to the emissivities of the boundary surfaces. Galvanized sheet metal has an emissivity equal to 0.25 and concrete and soils have emissivities between 0.90 and 0.94 (2). However, any smooth surface coated with enamel paint of any color has been found to have an emissivity equal to 0.96 (3). Therefore, the interiors of

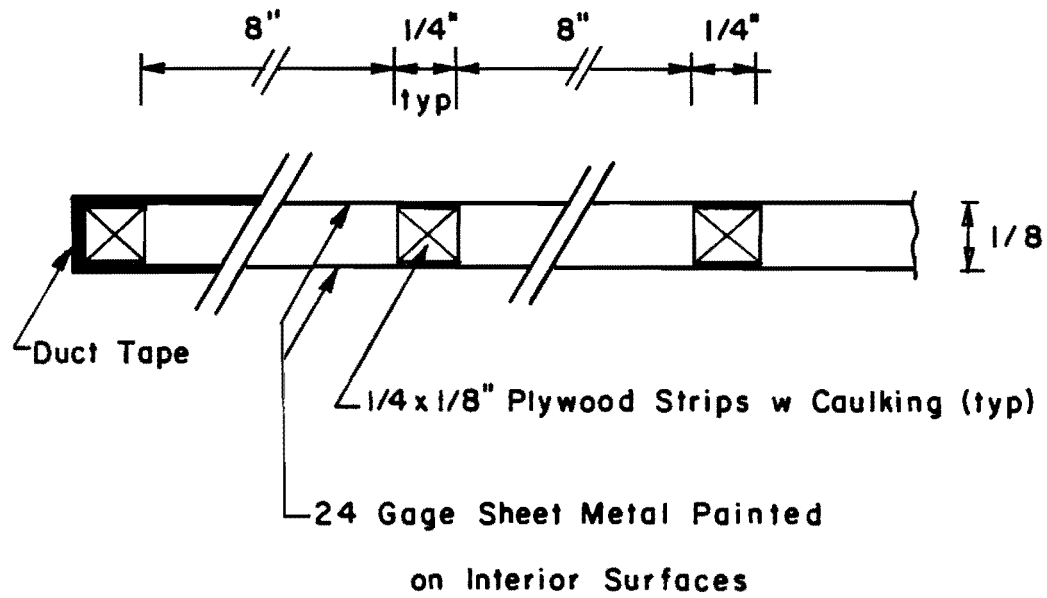
the voids were primed and painted prior to closure and sealing to eliminate the effect of lower surface emissivity.

To assure that the voids would remain open after the concrete was placed, direct load tests were performed on sample voids of 24 gage sheet metal to determine the maximum distance between supports. It was found that a distance of 8 in. between supports was the maximum allowable spacing that could be used. The selected cross section for a void is shown in Figure 3.6. Figure 3.7 shows a plan view of Void 1 as an example of void construction.

#### 3.4 Construction of the Experimental Slab

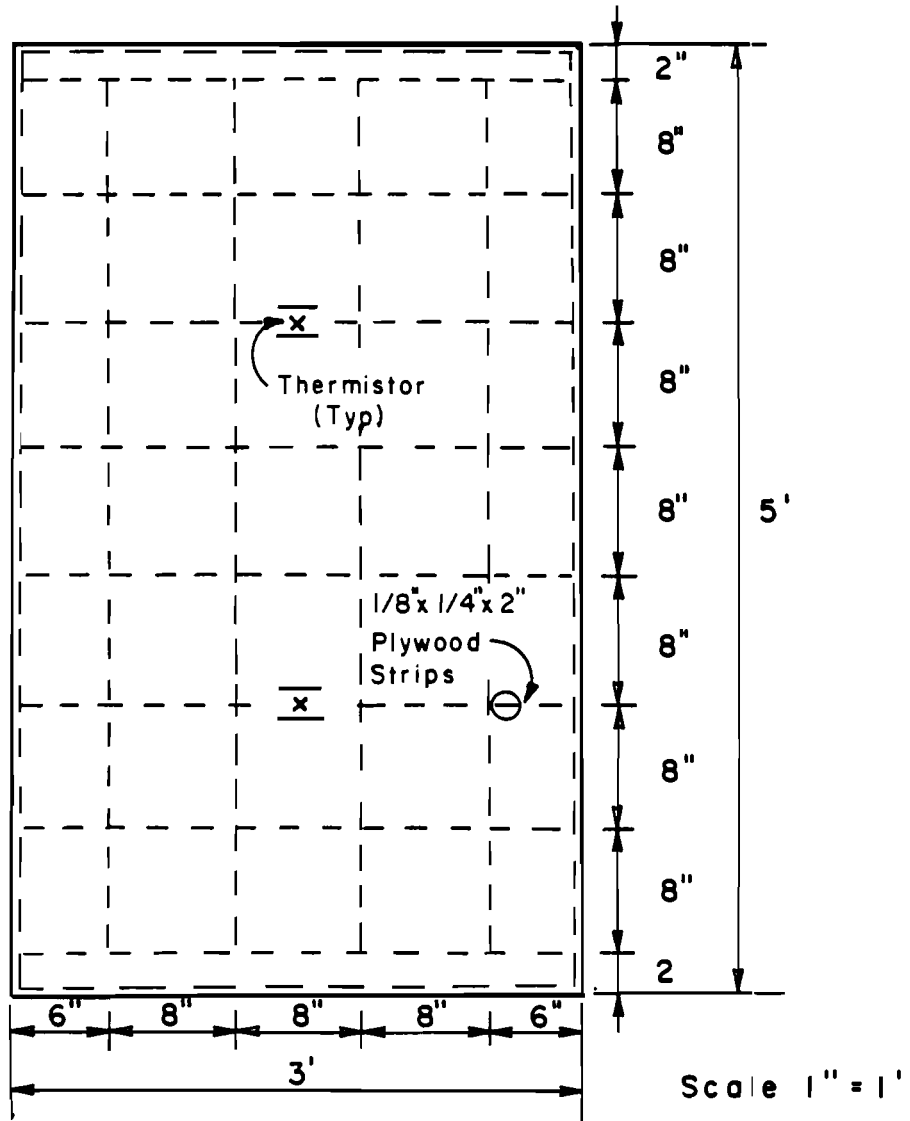
The site at Balcones Research Center behind Building 20 has a typical soil profile of 6 inches (15 cm) of topsoil followed by 1 to 2 ft (30 to 60 cm) of broken limestone mixed with soil. This is underlain with solid limestone. The excavation for the slab was carried out utilizing equipment and personnel from the maintenance department at BRC. The excavation was carried down to a depth of one ft 2 in. (35 cm) below the top of the slab grade and a 6-in. (15-cm) soil/cement mixture was compacted in place to provide a smooth work surface for the voids and concrete placement.

In order to install the soil thermistors, it was necessary to drill 1 1/2-in. (38-mm) diameter holes in the underlying limestone to a depth of 3 ft (91 cm) below sub-base grade. The four thermistors to be installed in each



(No Scale)

Figure 3.6. Cross section of a Void



Void 1

Void 2 and Void 3  
of Similar Design

Figure 3.7. Typical Void Design

hole (see Figure 3.4) were lowered into the hole and a dry sand was backfilled in 6-in. (15-cm) lifts. Each lift was watered down and compacted with a rod before the next lift was added. The lead wires from the soil thermistors were carefully buried in the sand subbase to avoid accidental damage.

Placement of the concrete thermistors was a delicate action. The fragile nature of the thermistor dictated some sort of protection against damage during the actual concrete placement. This protection, however, could not in any way interfere with the heat transfer around the thermistor. It was decided to cast each thermistor into a 1-in. (25-mm) diameter by 6-in. (15-cm) long concrete cylinder prior to placement in the field. In that way the thermistor would be less likely to be damaged and the surrounding protection had the same thermal properties as the slab. Each cylinder had a double strand of standard tie wire through it longitudinally. This provided an easy means for attaching the cylinders to the reinforcing steel in the slab. Mortar mix was used for the cylinders.

Plywood forms were then constructed and the voids placed in position on the subbase. The reinforcing steel was then laid in place and the concrete thermistors attached to rebars.

In the field, the thermistors used to measure the temperatures at mid-depth in the slab were wired directly to the rebar, which was at mid-depth. The thermistor cylinders used to measure temperatures at the lower surface of the slab were simply hung from the reinforcing steel.

Placing the surface thermistors was a special problem. It was reasoned that, due to usual construction tolerances, it would be difficult to place these thermistors within the required 1/8 in. (3 mm) of the surface. Therefore, lead wires were run vertically out from the trunklines and the surface thermistor connections were made after the slab was placed and cured.

When all the thermistors, voids, steel, and forms were in place, ready-mix concrete was ordered for the slab placement. A standard six-sack Class "C" Highway mix was used. Finishing was done using a screed board followed by hand troweling. The concrete was covered with burlap, and water was continuously sprinkled on it for ten days. Twenty-eight day concrete strengths averaged 4880 psi (340 kg/sq cm).

After the slab was cured, 1/2-in. (13-mm) wide grooves were chiseled into the surface of the slab to a depth of 1 1/2-in. (38-mm). The surface thermistors were connected to the wires protruding from the concrete and then grouted into the grooves using a 1:2 (cement:sand)

mortar mix. This allowed the thermistors to be placed within 1/8 in. (3 mm) of the slab surface.

The slab sat for six weeks after placing before temperatures were monitored, so that there would be no effect from the heat of hydration. This also allowed time for connecting the wires to the temperature monitoring equipment and for performing trial scans.

### 3.5 The Infrared Scanning System

The infrared scanning system employed in this study was the Texas Instruments RS-310 Airborne Infrared Mapping System (see Appendix 1).

Infrared scanners use a front-coated, rotating mirror to scan the ground along and to both sides of the path of travel. The speed at which a scanner travels provides the distance between the scan lines. The radiant energy received by the scanner is converted into light and recorded on photographic film. The film is moved at a rate proportional to the velocity and height of the scanner, producing the continuous photographic record of the radiant energy detected. The film used is 70-mm RAR 2498. An example of an infrared image from this study is shown in Figure 4.12.

The logistics of the experiment required that the scanner be placed on a truck-mounted frame (Figure 3.8)

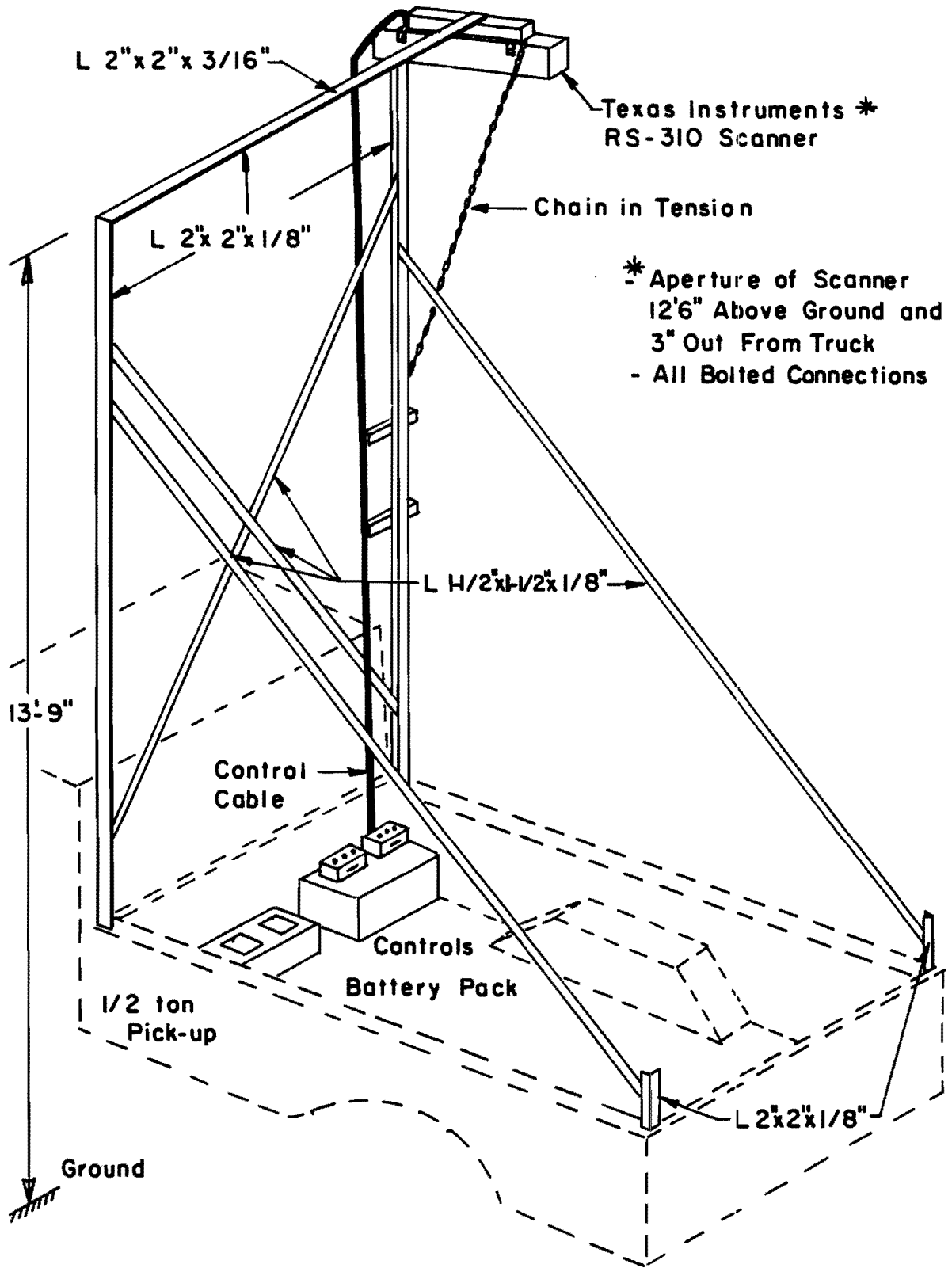


Figure 3.8. Truck Mount for Infrared Scanner

and driven alongside the site. From the geometry of the RS-310 scanner it was determined that it would have to be operated at a height of between 12 (3.7 m) and 14 (4.3 m) feet with a corresponding horizontal velocity of 3.5 ft/sec (107 cm/sec). The frame maintained the scanner at 12 feet 6 inches (3.8 m) above the ground. The truck used was able to sustain a velocity as low as 3.0 ft/sec (91 cm/sec) at low idle in first gear.

The scanner uses a Mercury-Cadmium-Telluride module which makes data collection in the 8 to 14 micron infrared wavelength possible. In this range, the radiant energy measured can be directly related to the surface temperature. The RS-310 is capable of discerning temperature differentials as small as  $0.2^{\circ}\text{F}$  ( $0.11^{\circ}\text{C}$ ). This compared favorably with the accuracy of the temperature monitoring system.

This page replaces an intentionally blank page in the original.

-- CTR Library Digitization Team

## CHAPTER 4. EXPERIMENTAL RESULTS

This chapter is presented in two parts. Section 4.1 presents the graphical results of the thermistor readings taken during the months of August, September, and October, 1980. Section 4.2 presents the images produced during the thermal scan on August 26, 1980. No discussion of the results is presented in this chapter. All analyses and comparisons are discussed in Chapter 5.

### 4.1 Temperature Data

The data presented in this section have been collected from various thermistor scans. Readings were taken on days with predominantly clear skies and low wind velocities. Of the 66 thermistors placed in the soil and concrete, eight have permanently malfunctioned. However, enough data were compiled from the remaining thermistors to produce recognizable trends and coherent results.

Table 4.1 shows the days and times when thermistor data were collected. The following sections (4.1.1 to 4.1.5) present the graphs monitored near the center of the slab.

TABLE 4.1 Thermistor Scan Schedule

Scan	Dates	First Reading	Final Reading	Weather Conditions	Remarks
1	8/22/80 to 8/23/80	9:30AM	3:30AM	Partly cloudy with some light rain near noon on 8/22. Max. temp = 101.5°F Min. temp = 81.5°F	Equipment malfunction at 3:30AM on 8/23.
2	8/25/80 to 8/26/80	8:30PM	12:00 Noon	Clear skies with light to moderate winds. Max. temp = 91.5°F Min. temp = 71.5°F	Infrared scan run every half hour from 6:30 AM to 11:00AM
3	9/5/80 to 9/6/80	7:30AM	5:00AM	Partly cloudy to clear with light winds. Max. temp = 97.8°F Min. temp = 76.0°F	Equipment malfunction at 5:00AM on 9/6.
4	10/2/80 to 10/4/80	12:00 Noon	12:00 Noon	Clear skies with light winds Max temp = 83.3°F Min. temp = 61.0°F	

TABLE 4.1 Thermistor Scan Schedule (continued)

Scan	Dates	First Reading	Final Reading	Weather Conditions	Remarks
5a	10/23/80 to 10/24/80	10:00AM	7:00AM	Partly cloudy to clear with light winds Max. temp = 79.8°F Min. temp = 53.0°F	Due to equip- ment malfunc- tion, data were not collected after 7:00AM on 10/24. The scan continued again at 7:00 AM on 10/25
5b	10/25/80 to 10/26/80	7:00AM	6:00AM	Clear skies with light winds. Max. temp = 72.0°F Min. temp = 44.7°F	

Due to on-going construction in the parking area adjacent to the slab, 2 inches of the west vertical edge had been uncovered prior to the patching of the asphalt. This resulted in substantial differences in the temperatures monitored at Stations D, F, and G. Preliminary analysis of these data has shown erratic behavior. For this reason, the authors do not consider these data valid and will not present them in this chapter or in the final analysis.

In order to reduce the amount of data presented here and to take advantage of the benefits of averaging, Stations B, C, and H have been averaged to produce graphs representing the temperature trends in the void systems. Likewise, Stations A, E, and J have been averaged to represent the solid system. Figure 4.1 is a graph of surface temperatures measured at Stations B, C, and H during scan 3. This graph shows the typical scatter that was encountered in the majority of the data. Based on this consistency, it appears reasonable to assume that the average temperature values presented in the following sections are valid.

4.1.1 Scan Number 1 - August 22-23, 1980. This scan was begun at 9:30 AM on August 22, 1980, under clear skies and with light southerly winds. The skies became partly cloudy around noon, and scattered showers fell in Austin

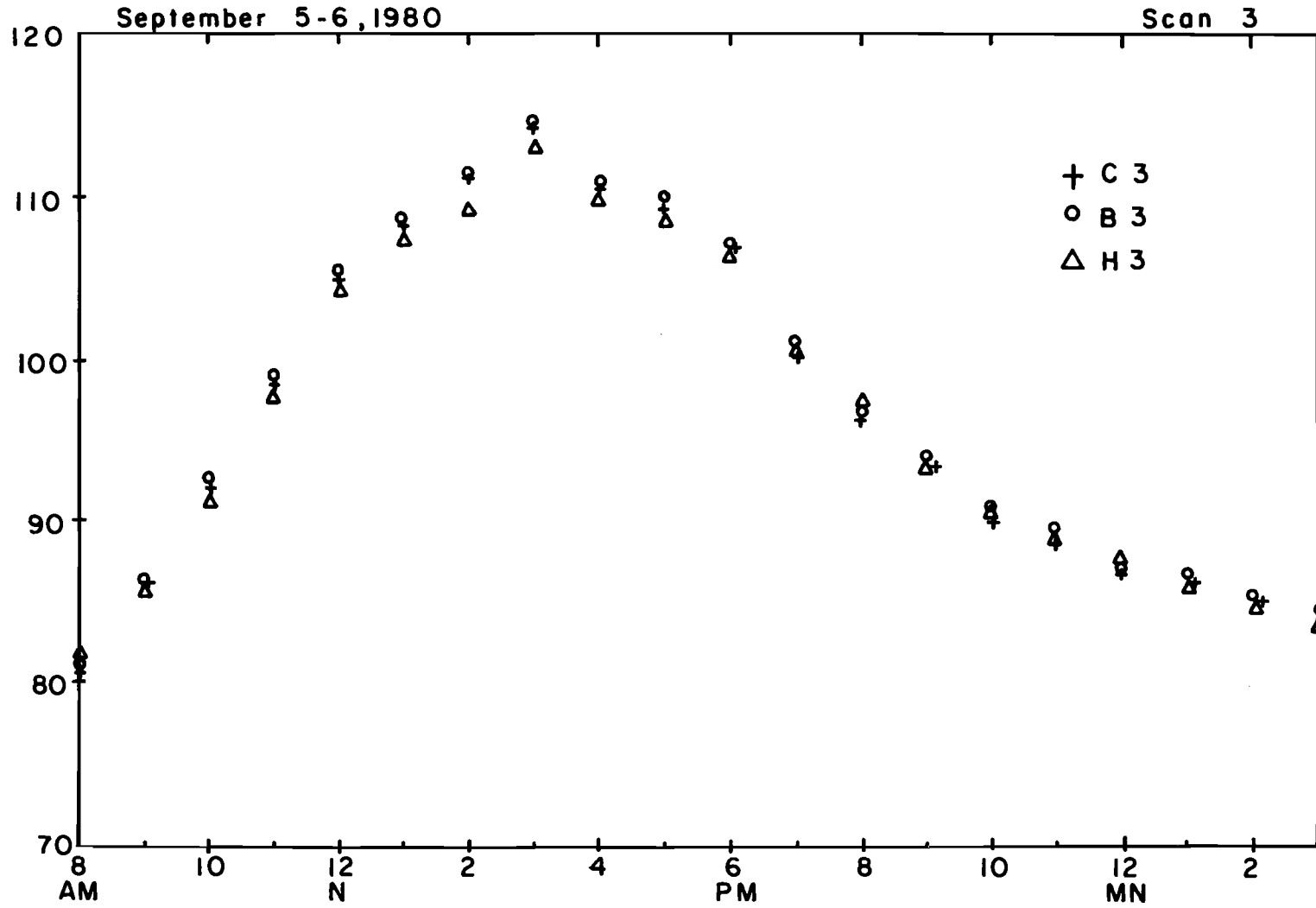


Figure 4.1. Typical Scatter of Surface Temperatures

between 1:00 PM and 6:00 PM. A few light showers fell at Balcones Research Center. The times of rainfall can be pinpointed by noting the interruptions on the surface temperature curves in Figures 4.2 and 4.3. All the surface curves show distinct drops around 1:30 PM, 3:30 PM, and 5:00 PM which indicate the cooling effect of the rain. Air temperature readings are also a bit erratic due to the effect of the rain and intermittent cloud cover.

4.1.2 Scan Number 2 - August 25-26, 1980. This scan was begun at 8:30 PM on August 25 under clear skies and with light variable winds. This scan was made in conjunction with an infrared thermal scan which began at 6:30 AM on August 26 and continued with a scan every half hour until 11:00 AM. The results of the thermal scan are reproduced in section 4.2.

Figures 4.4 and 4.5 are the graphs that represent the data collected during scan 2.

4.1.3 Scan Number 3 - September 5-6, 1980. This scan was begun at 7:30 AM on September 5, 1980. Skies were clear throughout the scan and winds were light to moderate. Figures 4.6 and 4.7 represent the data collected during this scan.

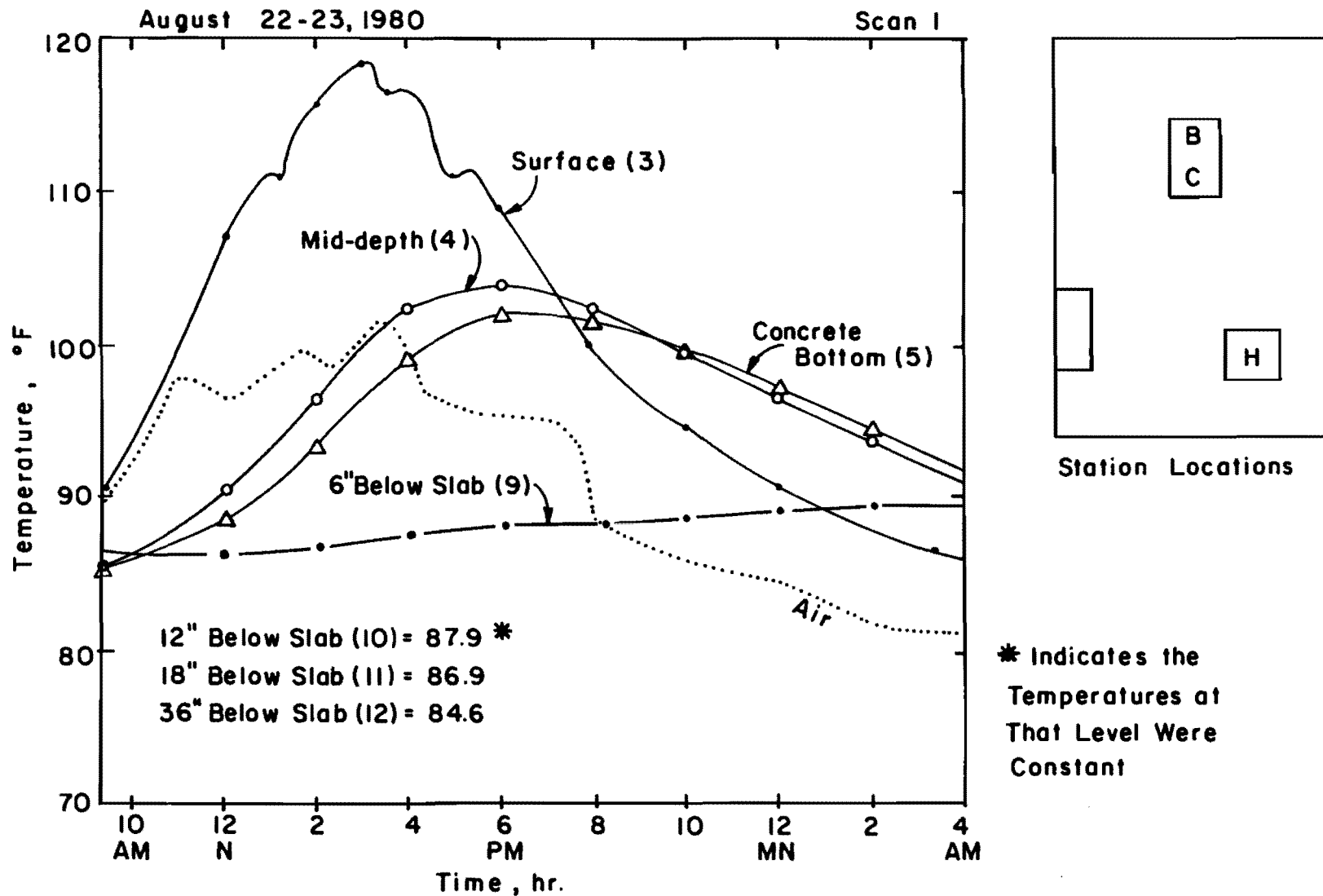
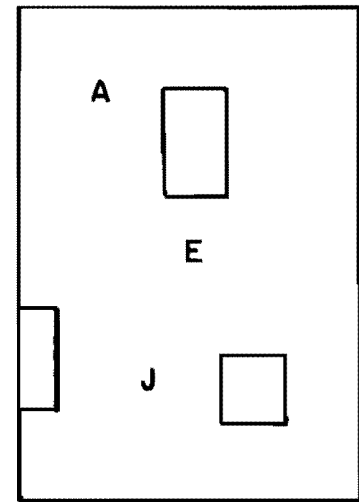
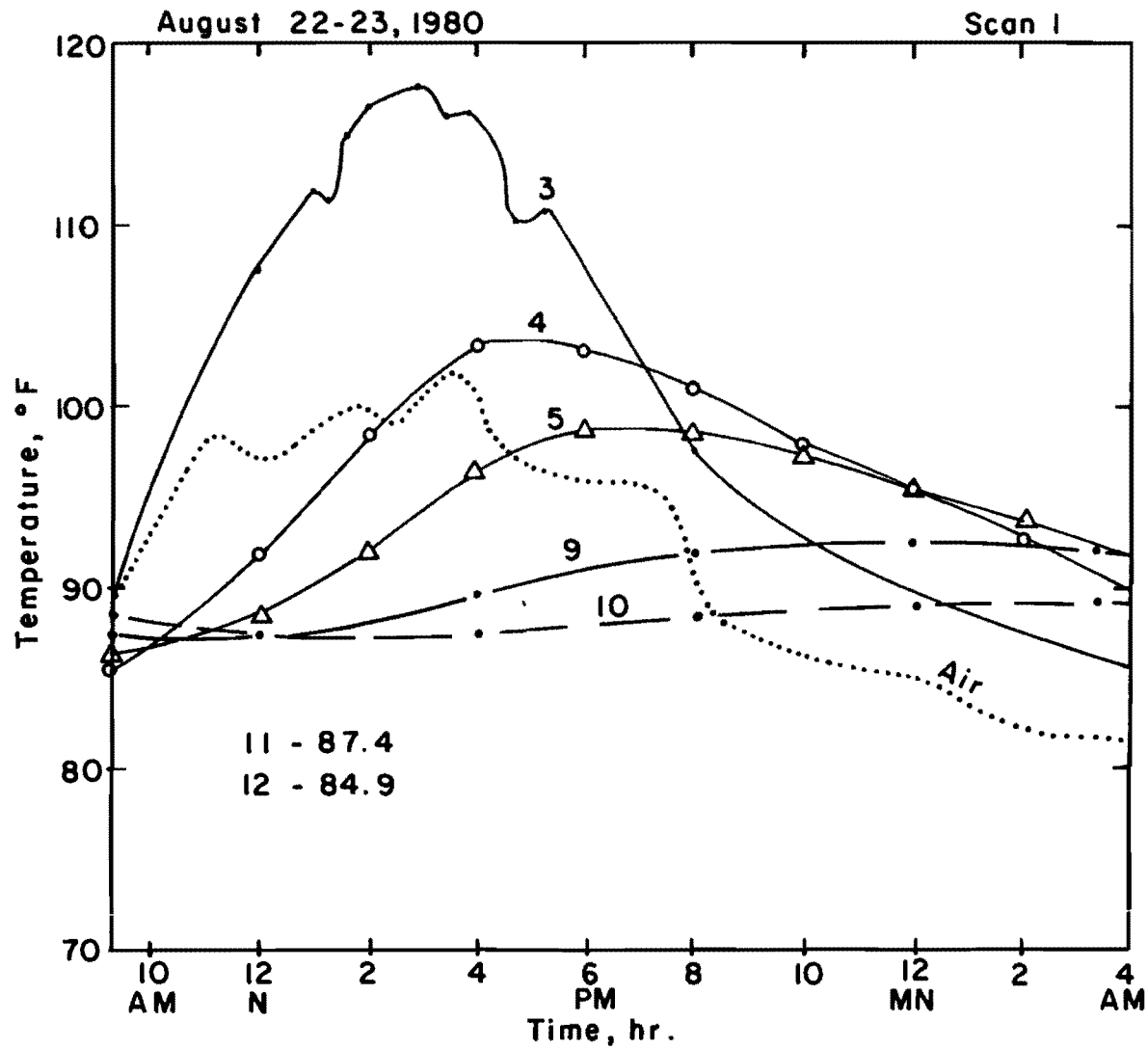


Figure 4.2. Temperatures of the Void System (Stations B, C, H)



Station Location

Figure 4.3. Temperatures of the Solid System (Stations A, E, J)

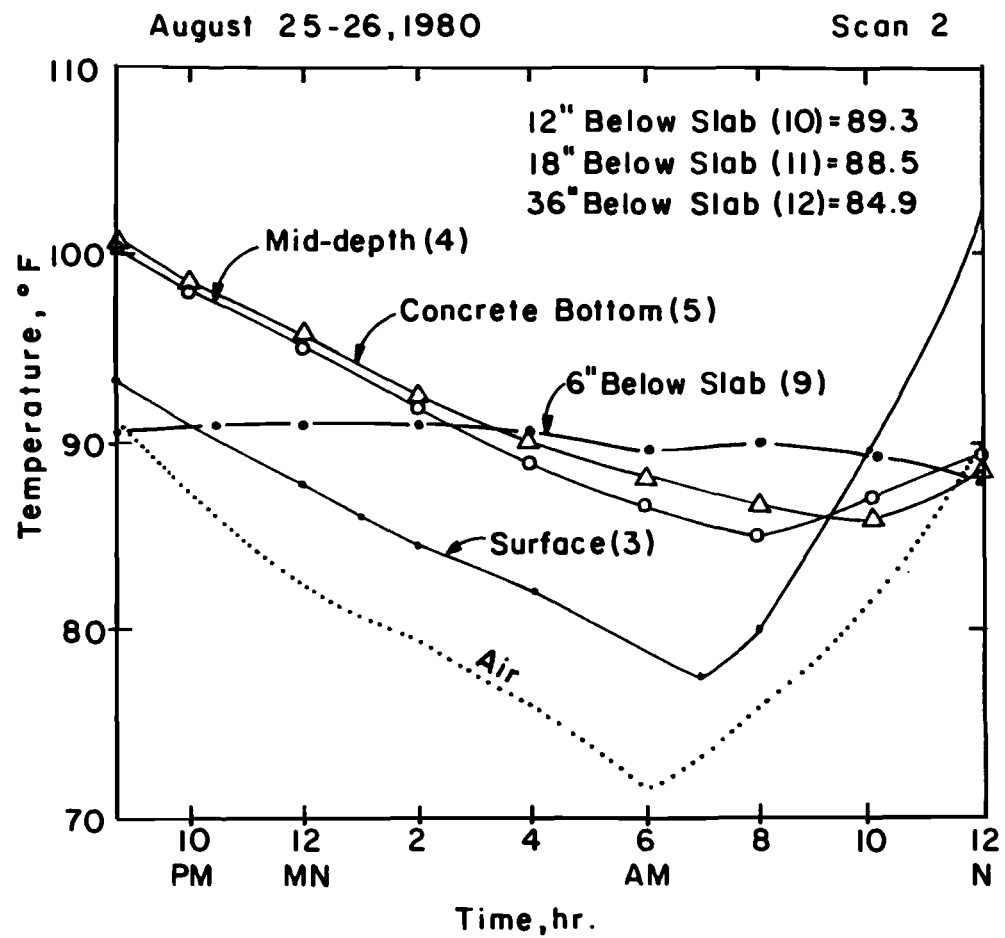


Figure 4.4. Temperatures of Void System (B, C, H)

August 25-26, 1980

Scan 2

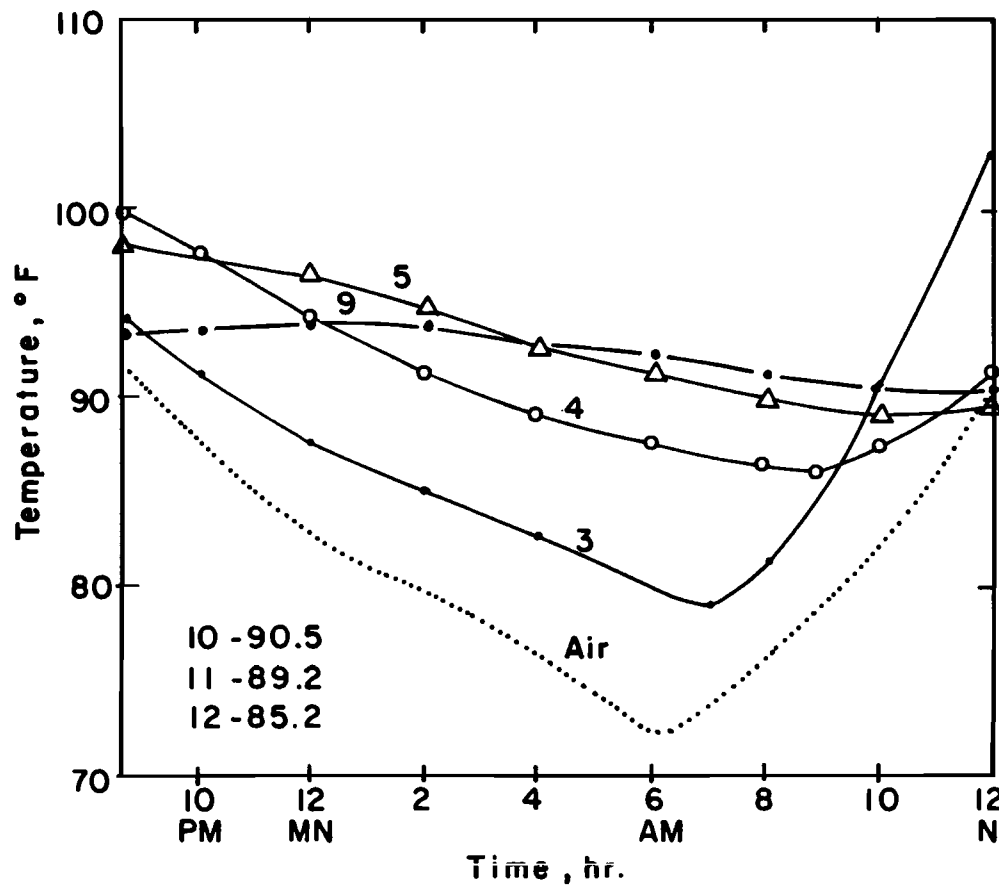


Figure 4.5. Temperatures of Solid System (A, E, J)

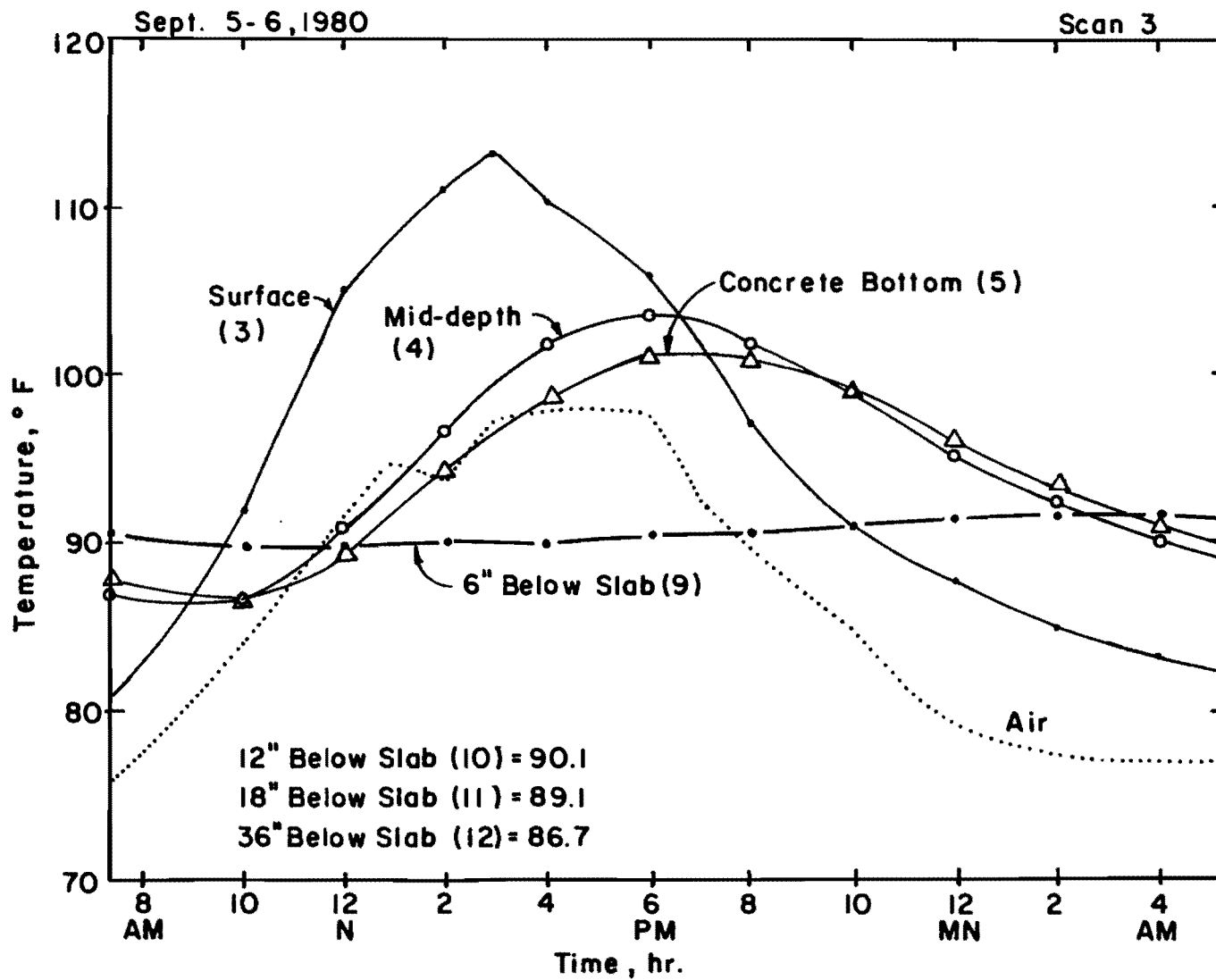


Figure 4.6. Temperatures of the Void System (B, C, H).

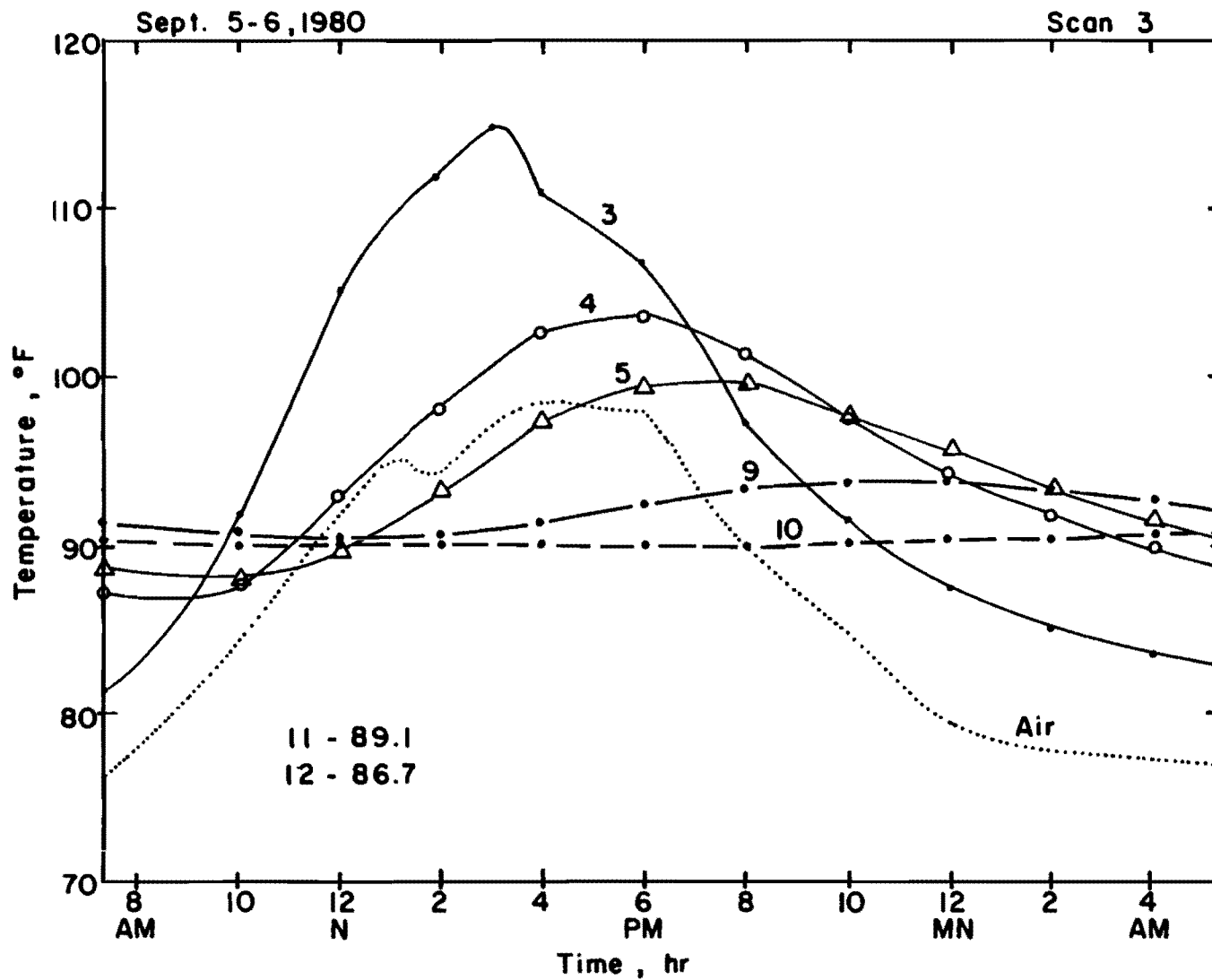


Figure 4.7. Temperatures of the Solid System (A, E, J)

4.1.4 Scan Number 4 - October 2-4, 1980. Preliminary analyses of the data from scans 1 to 3 showed a need for longer term monitoring to check for the repeatability of the data. For this reason, scan 4 is 48 hours long. It was begun at 12 Noon on October 2, 1980, and ended at 12 Noon on October 4, 1980. Skies were predominantly clear and there were light, variable winds. Figures 4.8 and 4.9 present the data collected on these days in graphical form.

4.1.5 Scan Number 5 - October 23-26, 1980. This scan was begun at 10:30 AM on October 23, 1980. It was interrupted at 7:00 AM on October 24 by an equipment malfunction. This was rectified at 7:00 AM on October 25, and the scan was continued until 6:00 AM on October 26.

The morning of the first day was cloudy until about noon. Moderate winds developed at this time. The morning of October 25 was exceptionally clear and cold with only light, intermittent winds. It remained clear the entire day and night. Figures 4.10 and 4.11 show this data in graphical form.

#### 4.2 Results from Infrared Thermography

The only infrared scan performed in conjunction with this study was done on August 26, 1980. The first scan was made at 6:30 AM and subsequent scans were made every half hour until 11:00 AM.

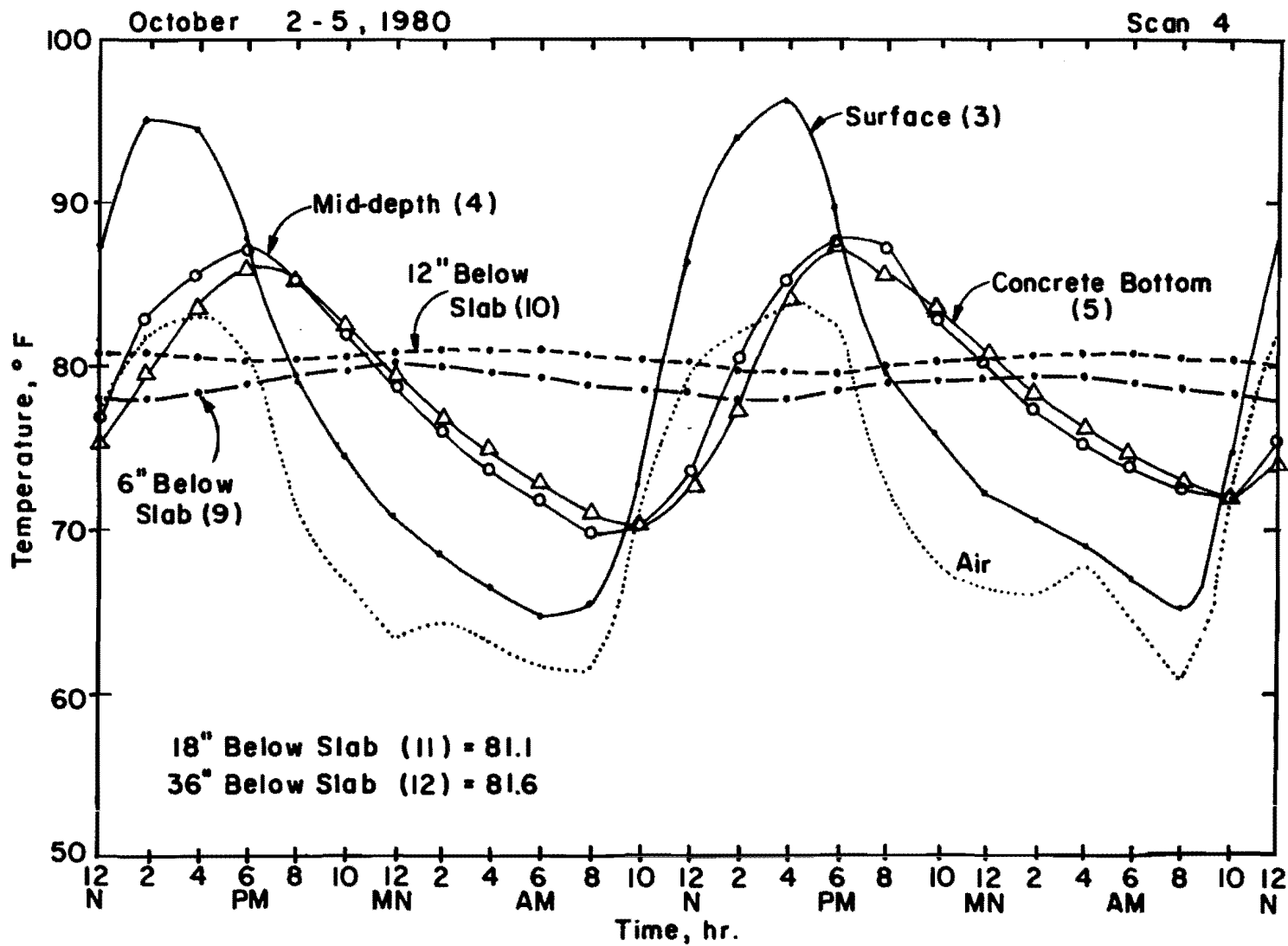


Figure 4.8. Temperatures of the Void System (B, C, H)

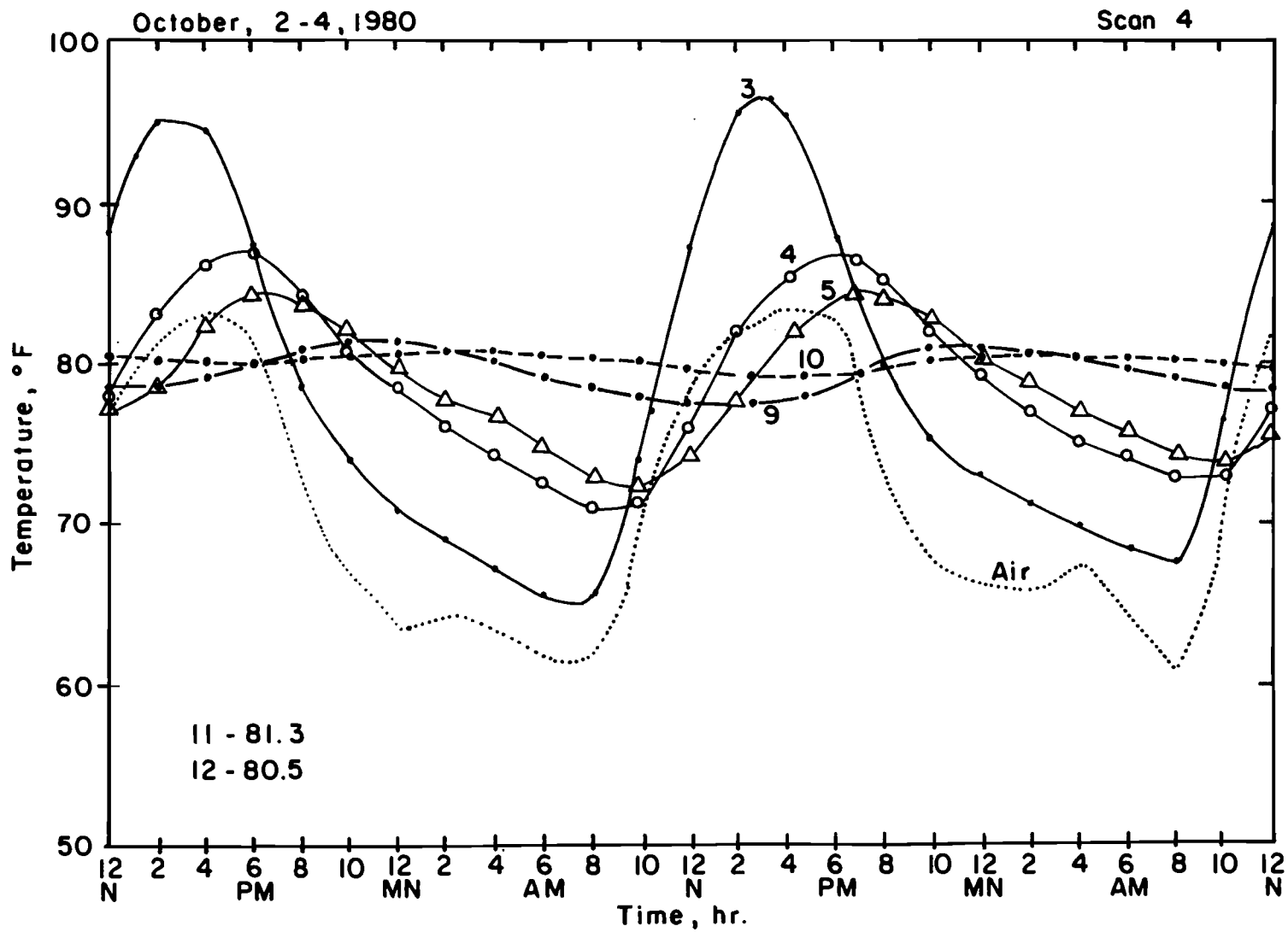


Figure 4.9. Temperatures of the Solid System (A, E, J)

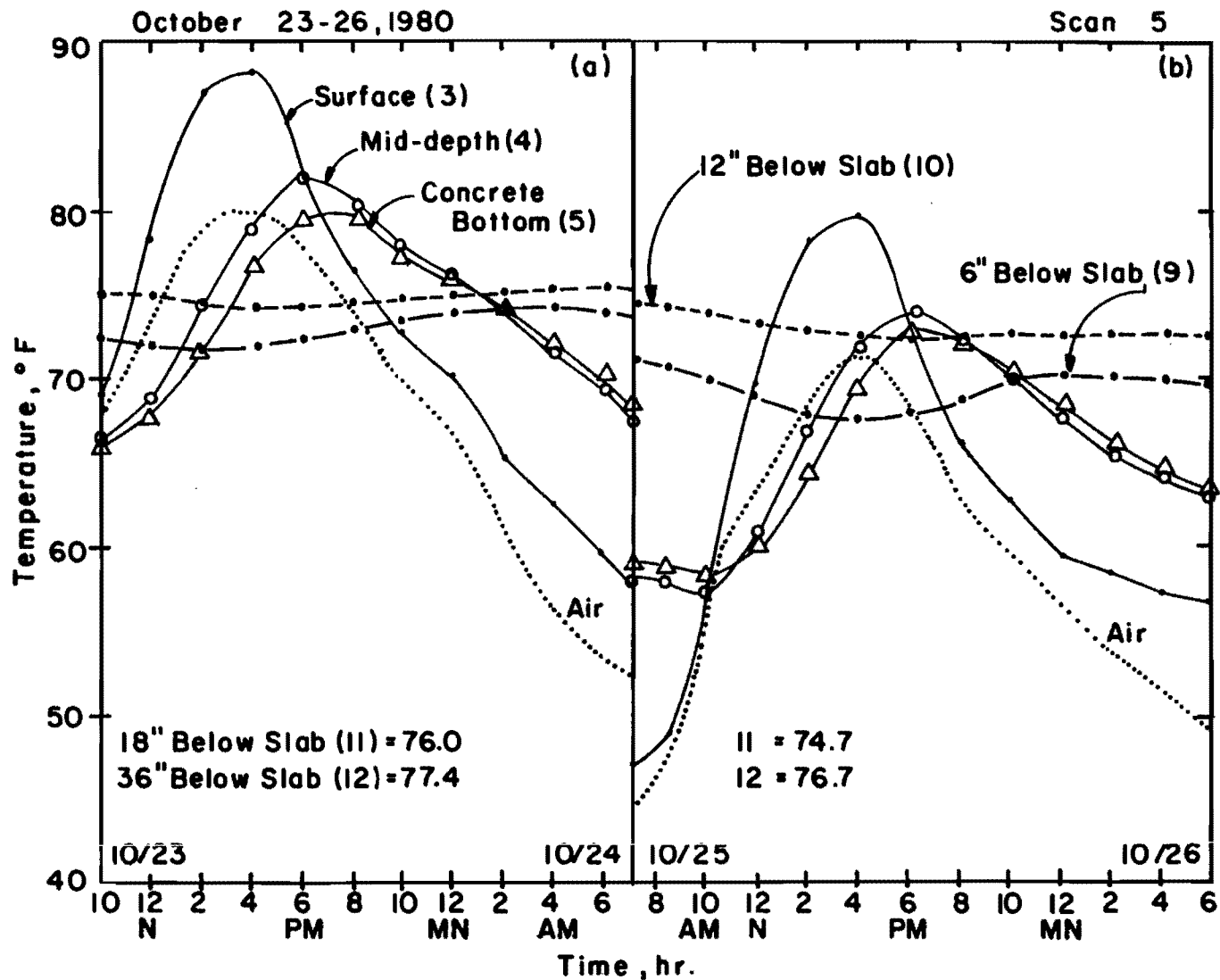


Figure 4.10. Temperatures of the Void System (B, C, H)

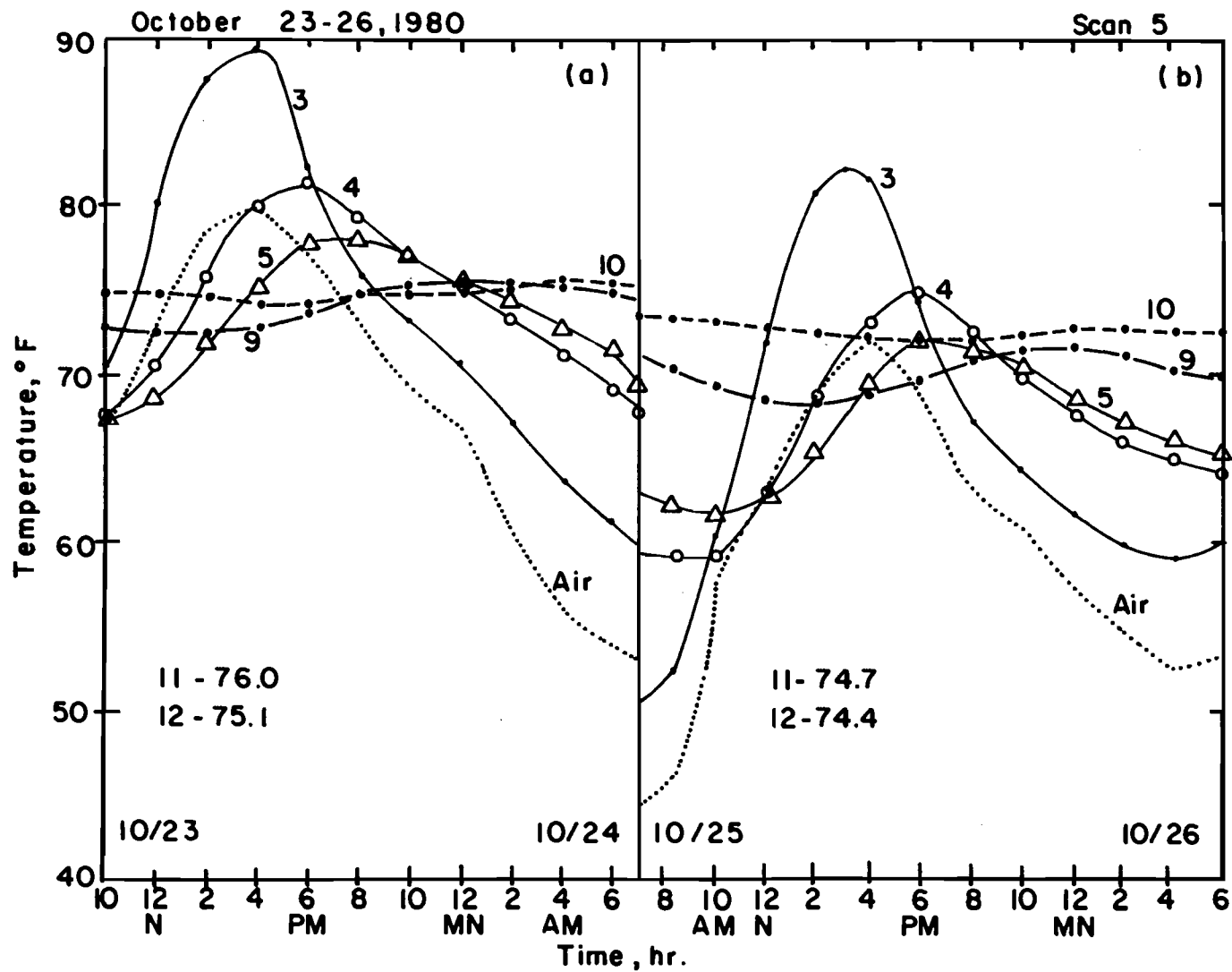


Figure 4.11. Temperatures of the Solid System (A, E, J)

Figures 4.12 to 4.14 show some of the images produced during this scan. The scale in the long direction of the slab has been distorted. This is attributed to a truck speed slower than needed. The obvious, long thin marks on the slab surface correspond to the grooves that were chiseled into the surface for the placing of the surface thermistors. The grout used to fill the grooves has a slightly different emissivity and, therefore, produces a different shade of gray than the rest of the slab. These marks should be ignored when the images are interpreted.

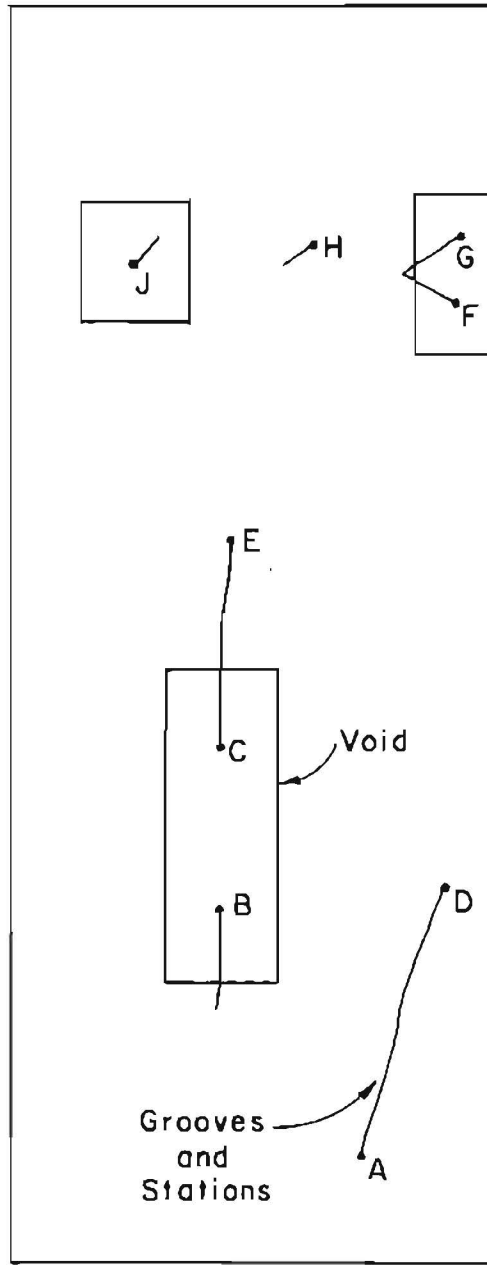
The east and west edges of the slab are not well defined. On the eastern edge, this is due to an accumulation of dust and some grass overgrowth adjacent to the slab. On the western edge, the asphalt for the parking area had not yet been placed, leaving about 2 inches of the vertical edge uncovered. Both of these conditions produced substantially lower surface temperatures, which show very dark in the image and obscure the edge of the slab.

Figure 4.12 shows the image produced at 6:30 AM along with a same-scale drawing of the slab and void locations.

Figures 4.13 and 4.14 are the images produced at 9:02 AM and 10:05 AM, respectively. The shadows that appear on these images are from the instrument shelters located east of the slab.



(a) Thermal Image



(b) Same Scale Diagram

FIGURE 4.12. IRT Scan - 6:30AM

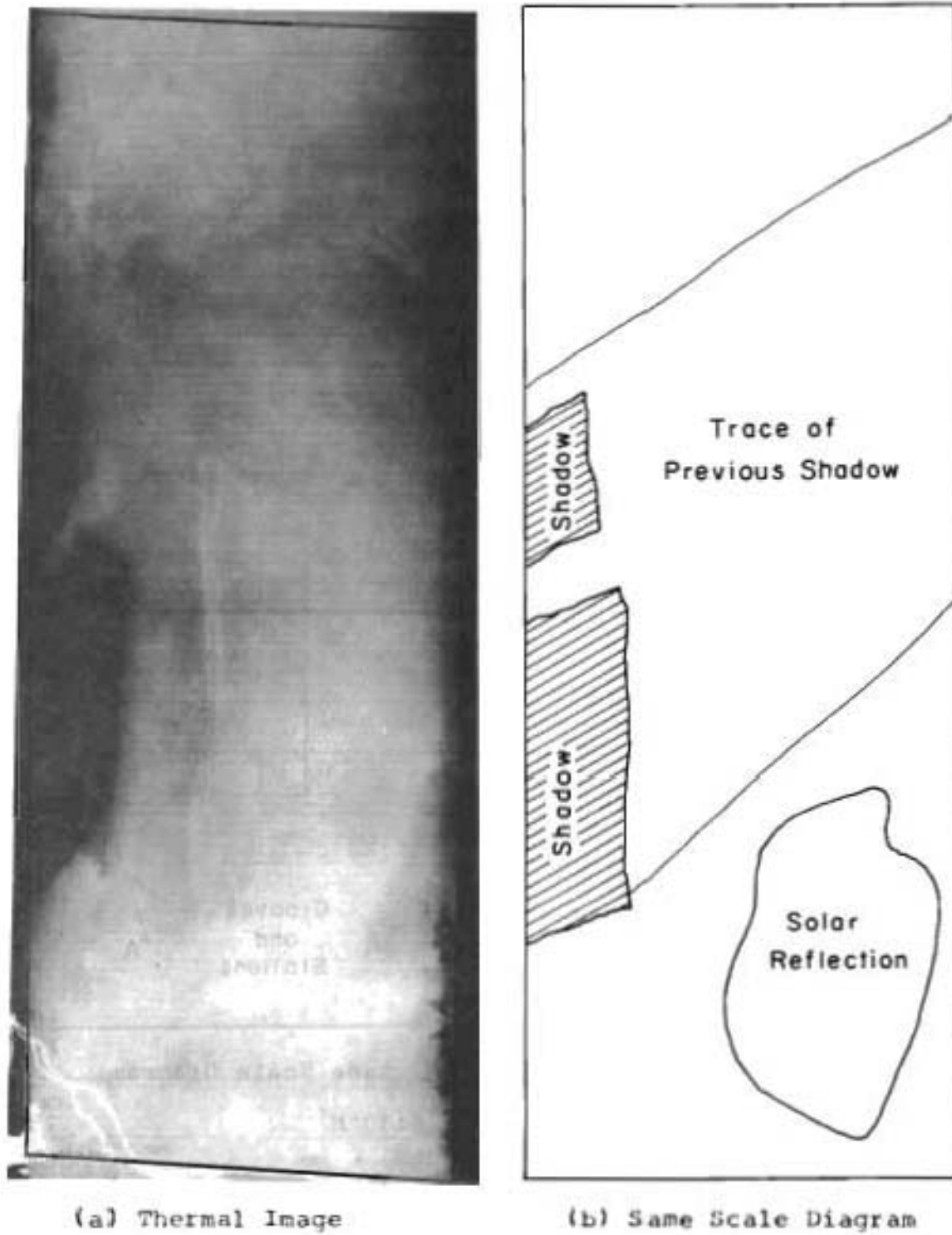
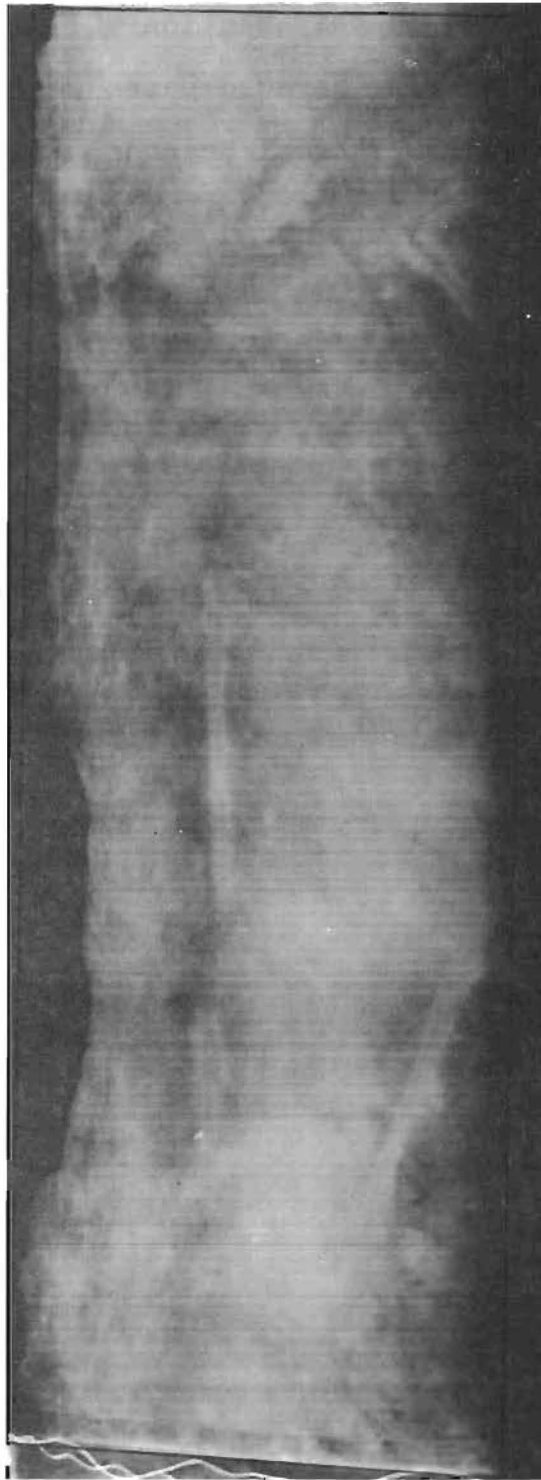
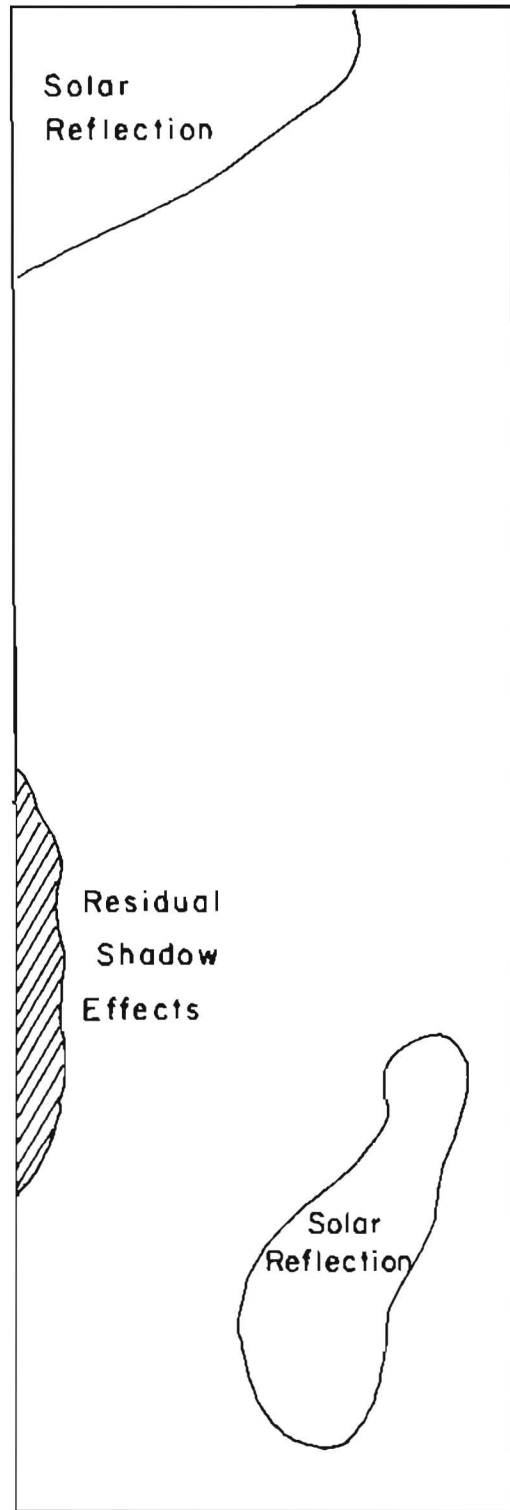


FIGURE 4.13. IRT Scan - 9:02AM



(a) Thermal Image



(b) Same Scale Diagram

FIGURE 4.14, IRT Scan - 10:05AM

No other images are reproduced in this section since light leakage into the film magazine damaged parts of most of the other images. The RS-310 Thermal Scanner is normally enclosed in a box in an airplane. It is not designed to be operated in direct, bright sunlight. However, a few simple modifications could be made to avoid this problem in the future.

## CHAPTER 5. ANALYSIS OF RESULTS

The primary concern of this study has been the effect that a void has on surface concrete temperatures. Chapter 2 presented the theoretical analysis that predicts the trends of surface temperature differentials using a heat transfer model under steady-state conditions. The radiation balance model further identifies some of the heat transfer mechanisms at work in the slab-void-soil and the slab-soil systems.

The results of the thermistor temperature measurements and the thermal scans described in the previous chapter provide the evidence to evaluate these theories and predictions. The data collected assist in clarifying the effect of the actual dynamic heat transfer conditions as compared to the steady-state model.

### 5.1 Thermistor Data

This section concentrates on the temperature differentials recorded between void and solid systems in the center of the slab. The temperatures monitored on the west edge of the slab are not considered in this analysis

because of the distortion effects from the uncovered edge, as discussed in Chapter 4.

To produce the graphs shown in Figures 5.1 to 5.5, the temperatures at Stations B, C, and H were averaged to yield a value for the void system temperature ( $T_{\text{void}}$ ) at the surface, mid-depth concrete and 6 inches below the slab. The readings at Stations A, E, and J were likewise averaged to give values for the solid system ( $T_{\text{solid}}$ ) at the same three levels. The solid system temperatures were then subtracted from the void system temperatures and plotted against time.

The five scans included in this analysis were taken during two different temperature regimens. Scans 1 to 3 were taken on days typical of the summer season in central Texas. The temperatures in scans 4 and 5 are more typical of autumn weather. As can be expected, the trends observed in these two different cases are distinct in some ways. However, they do provide a pattern useful for further work in void detection.

The temperatures monitored at all three levels showed substantial differentials between the void and solid systems. Figures 5.1 to 5.5 are the graphs of the temperature differentials versus time for the levels 3, 4, and 9 in scans 1 to 5.

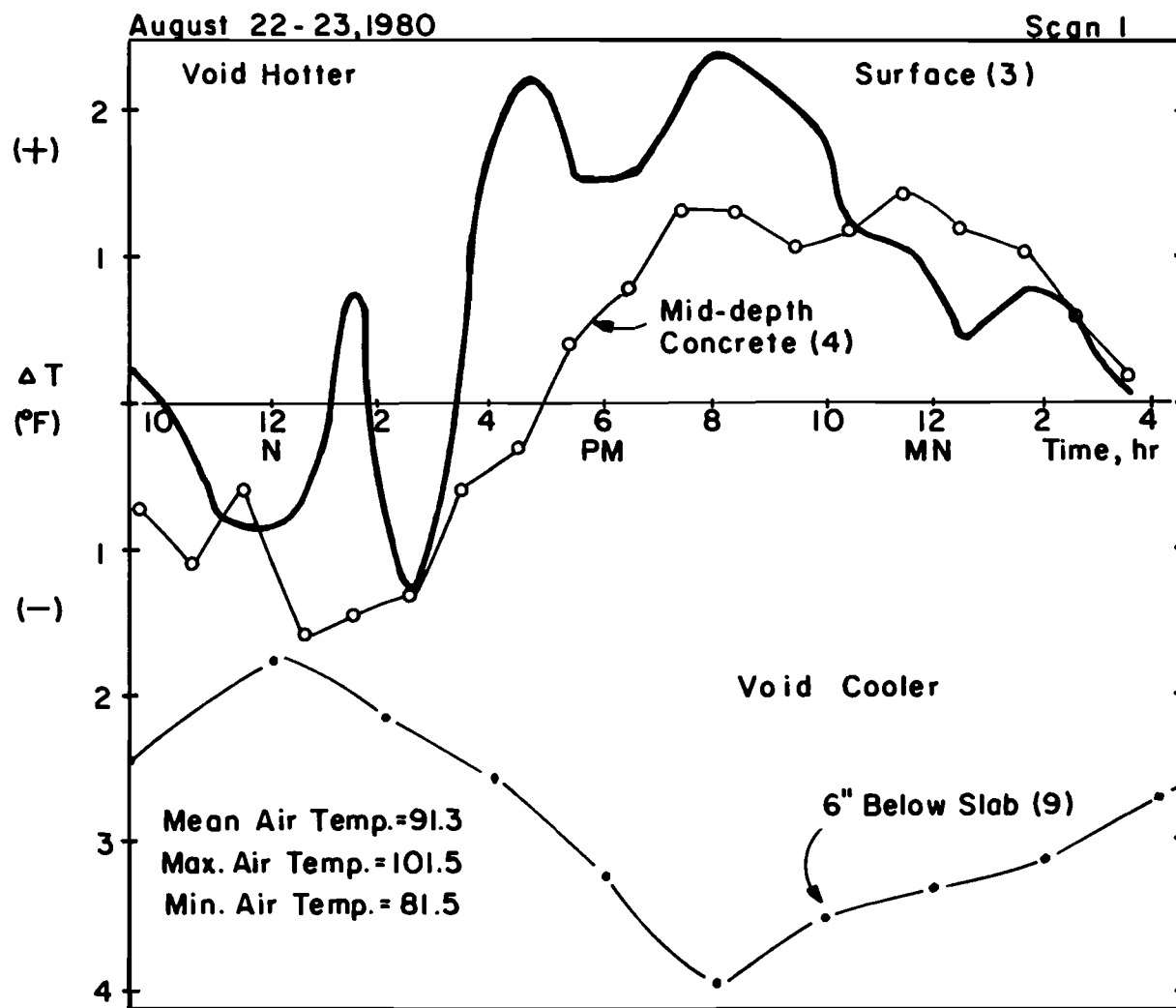


Figure 5.1. Values of  $\Delta T = T_{\text{void}} - T_{\text{solid}}$  at Levels 3, 4, and 9

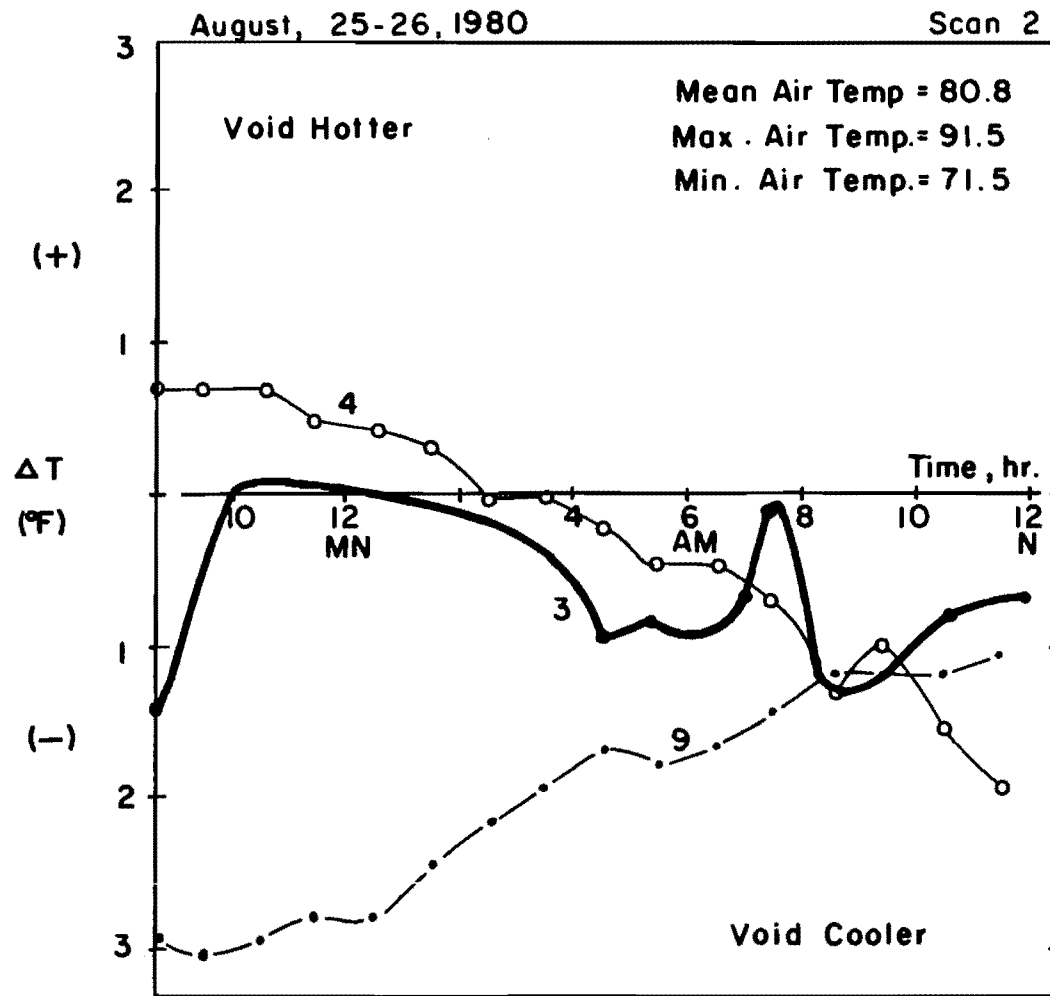


Figure 5.2. Values of  $\Delta T = T_{\text{void}} - T_{\text{solid}}$  at Levels 3, 4, and 9

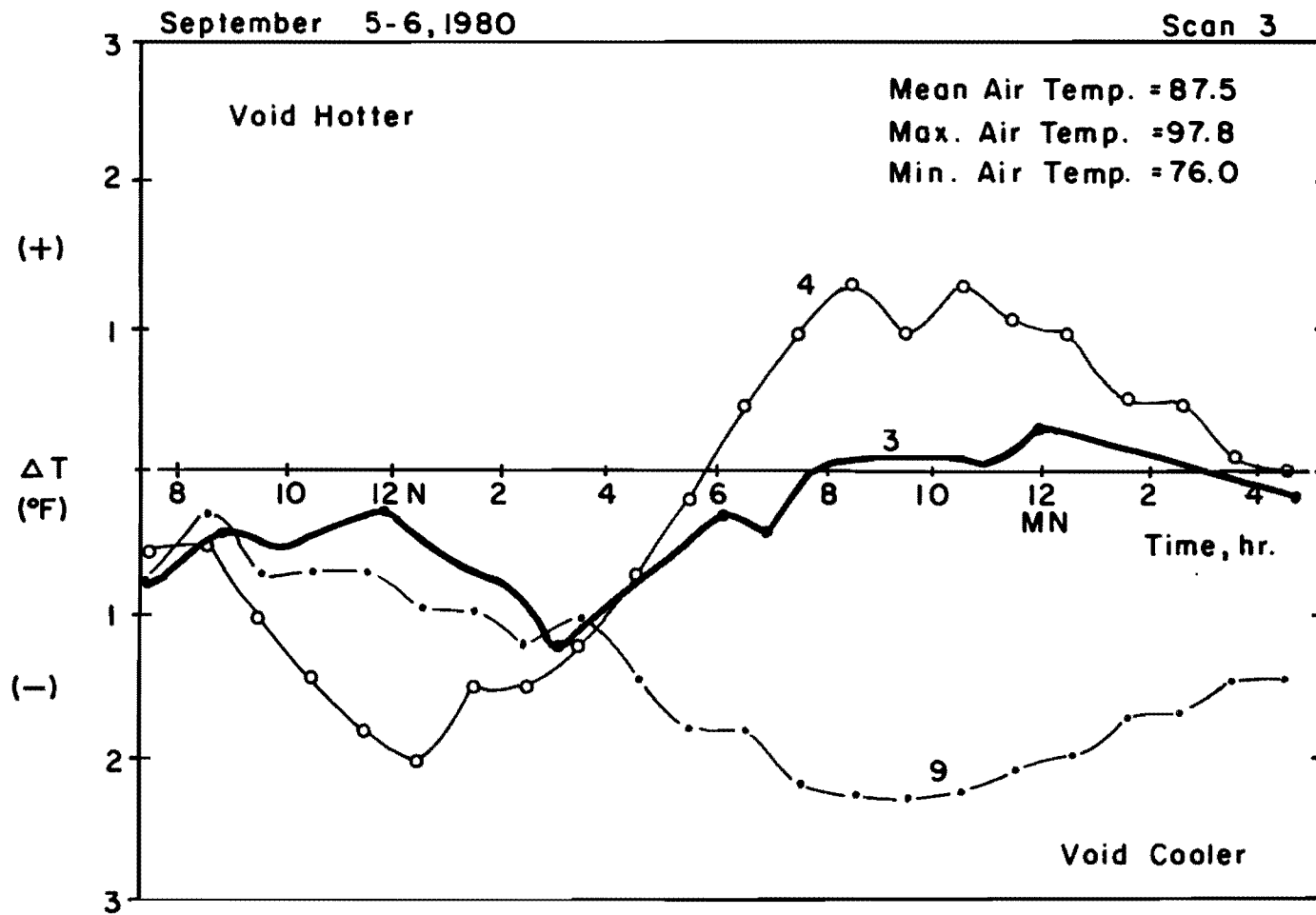


Figure 5.3. Values for  $\Delta T = T_{\text{void}} - T_{\text{solid}}$  at Levels 3, 4, and 9

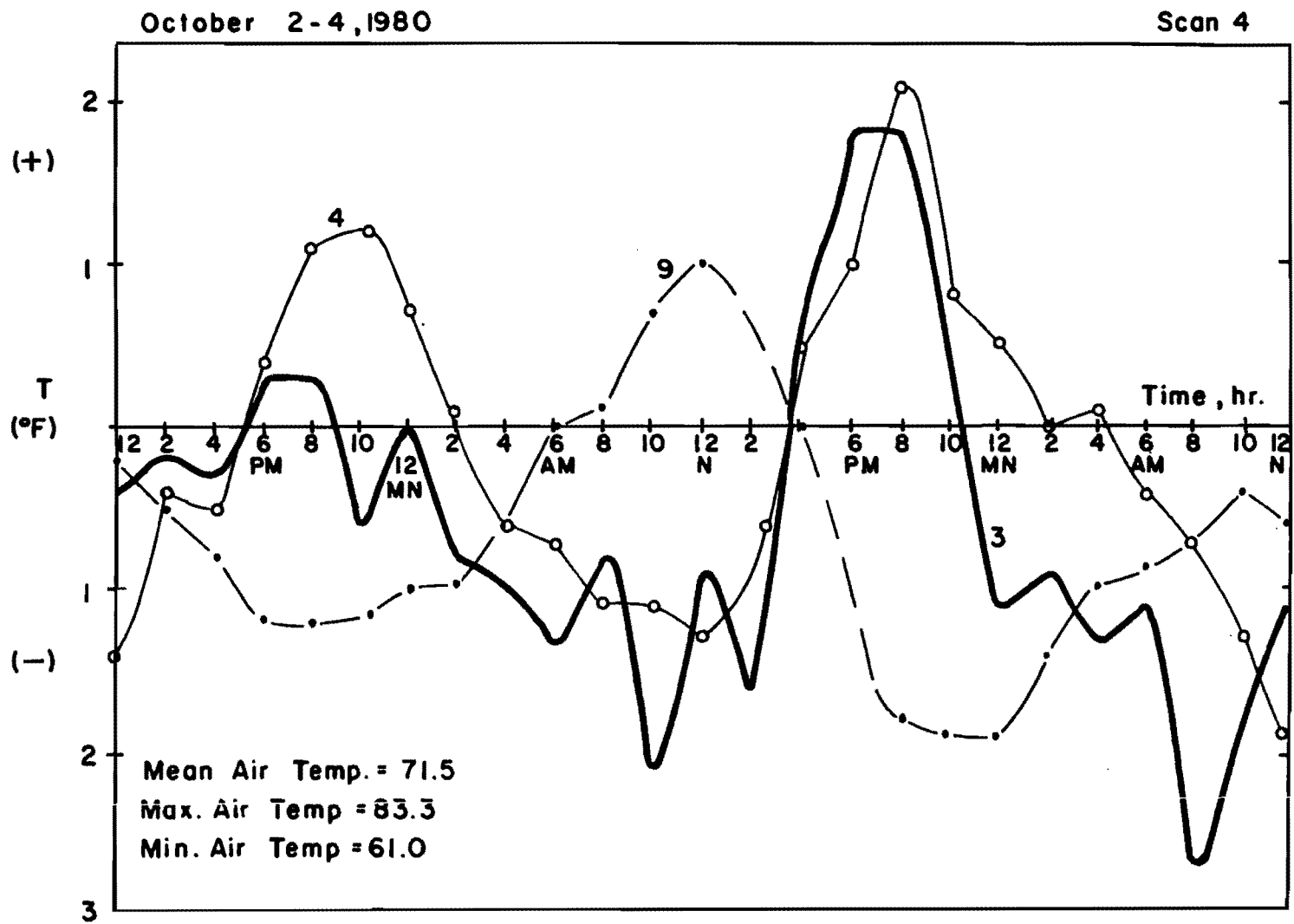


Figure 5.4. Values for  $\Delta T = T_{\text{void}} - T_{\text{solid}}$  at Levels 3, 4, and 9

October 23-26, 1980

Scan 5

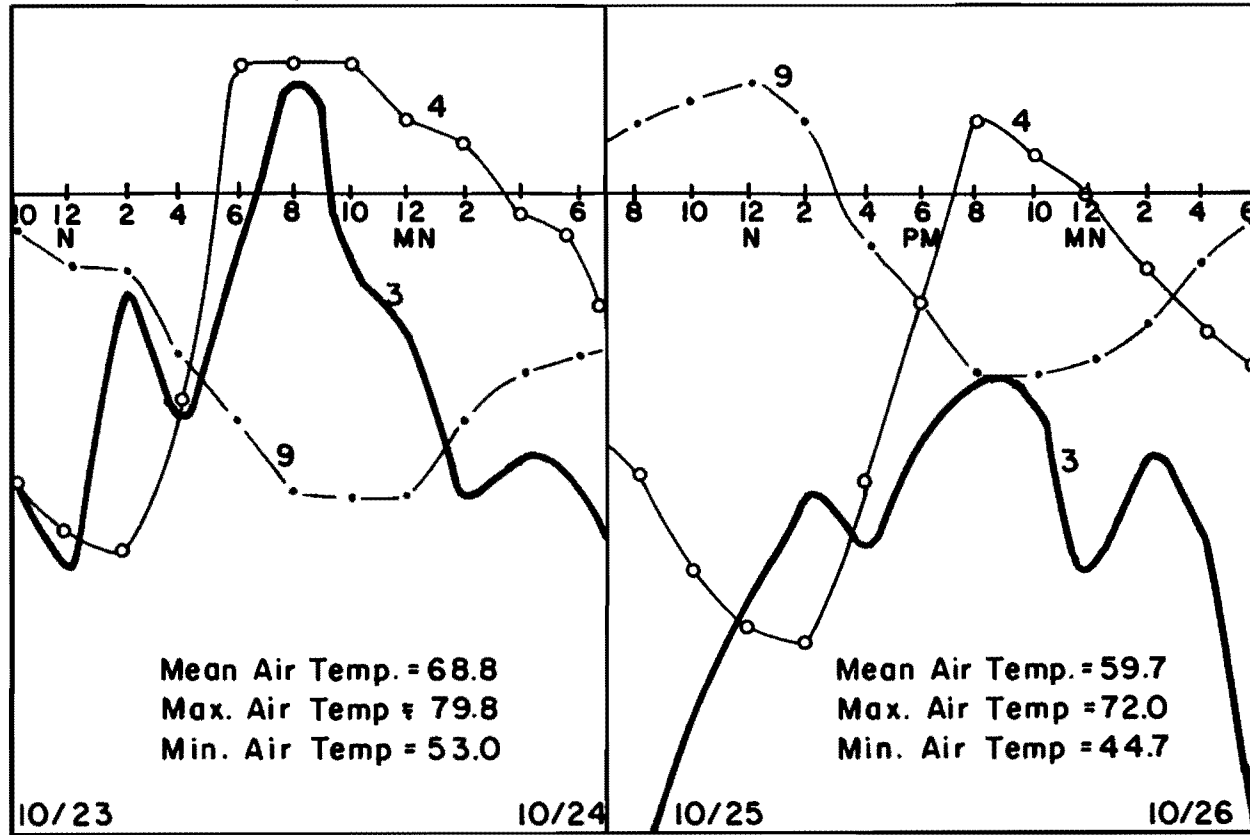


Figure 5.5. Values for  $\Delta T - T_{\text{void}} - T_{\text{solid}}$  at Levels 3, 4, and 9

### 5.1.1 Surface and Mid-depth Temperature Data.

The surface and mid-depth curves follow similar patterns, reaching maximum positive values during the night and maximum negative values during the day. The mid-depth curve, however, is much smoother and consistent. This is attributed to the additional parameters that can affect surface temperatures, such as wind, cloud cover, and differences in surface roughness. These localized differences in surface characteristics and environmental conditions are diffused as the heat travels down through the concrete mass and are not evident at mid-depth. However, the fact that the mid-depth curve follows the same general pattern as the surface curve demonstrates the validity of the temperature data.

Of particular importance for IRT is the magnitude of the temperature differentials monitored at the surface. Scan number 1 (Figure 5.1) shows maximum positive differentials of  $2.4^{\circ}\text{F}$  ( $1.3^{\circ}\text{C}$ ) occurring between 4:00 PM and 9:00 PM. Maximum negative differentials of  $1.2^{\circ}\text{F}$  ( $0.7^{\circ}\text{C}$ ) occur between 11:00 AM and 3:00 PM.

Scan number 2 (Figure 5.2) is conspicuous for the small differentials monitored. This is attributed to strong winds during the night of August 25-26. By morning, the winds had calmed and a distinct temperature differential began to appear. At the time of the thermal scan, between

6:30 AM and 11:00 AM, the surface temperature differentials were between  $-0.9$  and  $-1.3^{\circ}\text{F}$  ( $-0.5$  to  $-0.7^{\circ}\text{C}$ ). This difference in temperature was picked up by the thermal scan, as is shown in Figure 4.12.

Scan number 3 (Figure 5.3) shows a good differential occurring in the early morning hours before sunrise of between  $-0.5$  and  $-1.3^{\circ}\text{F}$  ( $-0.3$  to  $-0.7^{\circ}\text{C}$ ). During the daylight hours, there is very little difference in temperatures between the two systems. The winds were light the entire day and probably are not the reason for this change. However, it rained for two days prior to this scan. This most certainly raised the moisture content of the concrete. Water is a good conductor of heat and would have the effect of more quickly evening out the temperature differentials created by the voids.

Scan number 4 (Figure 5.4) shows a very distinct trend in the surface and mid-depth differentials. A maximum positive reading of  $1.8^{\circ}\text{F}$  ( $1.0^{\circ}\text{C}$ ) was obtained between 5:00 and 8:00 PM on October 4. The previous day a positive maximum of lesser value,  $0.3^{\circ}\text{F}$  ( $0.2^{\circ}\text{C}$ ) was observed during the same hours. Maximum negative values of between  $2.0$  and  $2.7^{\circ}\text{F}$  ( $1.1$  to  $1.5^{\circ}\text{C}$ ) were observed on both nights, with the maximum values occurring at around 9:00 to 10:00 PM.

Scan number 5 (Figure 5.5) shows similar trends on the two days monitored. A significant difference is

noted between the two days. The surface differential curve, though similar in shape, is shifted downward about  $1.5^{\circ}\text{F}$  ( $0.8^{\circ}\text{C}$ ) on October 25-26 as compared to October 23-24. This is due to the very low temperatures that occurred during the early morning of October 25. The air temperature was  $44.7^{\circ}\text{F}$  ( $7.1^{\circ}\text{C}$ ) at 7:00 AM. Maximum negative differentials of  $3.4^{\circ}\text{F}$  ( $1.9^{\circ}\text{C}$ ) were monitored in the early morning (8:00 AM on October 25 and 6:00 AM on October 26). The curves were entirely negative except for a short period around 8:00 PM on October 23. This indicates the effect that the rapidly changing, seasonal air temperatures have on the heat transfer in the concrete. This effect is further magnified by the fact that the soil mass below the slab is not changing its average temperature as quickly as the air is.

Figure 5.6 shows a common graph of the surface temperature differentials for the seven 24-hour scans included in this study. All seven scans are plotted against the same 24-hour time period. All of the curves follow the same general pattern. The maximum values consistently occur between 6:00 and 10:00 PM, with the minimum values occurring between 4:00 and 8:00 AM. The average of the seven curves clearly illustrates the sinusoidal pattern observed.

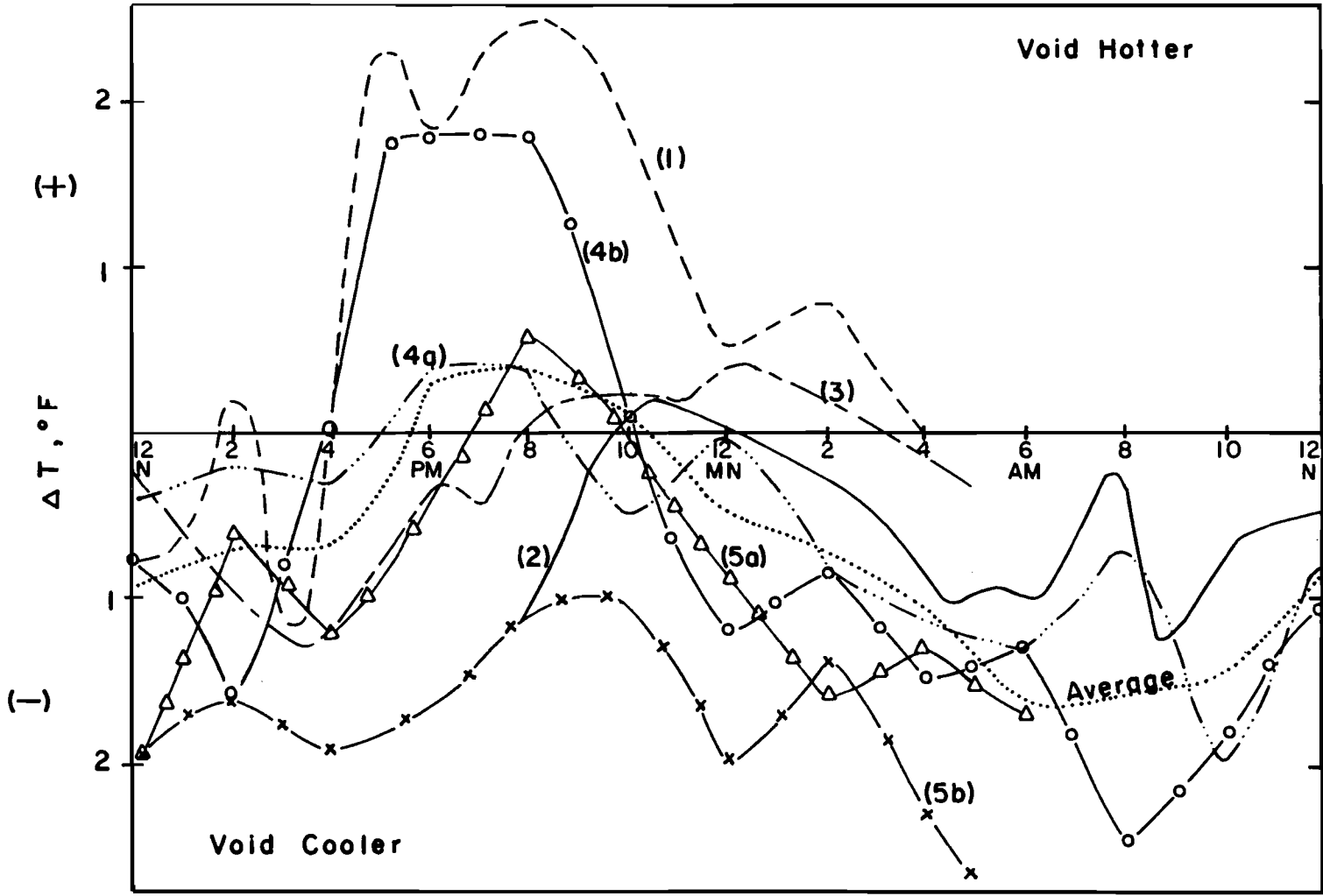


Figure 5.6. Average Surface Temperature Differentials

Although all seven curves in Figure 5.6 follow the same pattern, there is considerable variation in their peak values. Curves 1 and 4b are distinct for the high positive values monitored during the early evening, while curve 5b is distinct for always remaining in the negative zone. The rest of the curves lie in a zone running roughly parallel to the average curve. These variances in magnitude of the peak values are attributed to the different climatic conditions that existed for each scan. Despite these varying conditions, however, all the curves show large negative differentials in the early morning hours between 4:00 and 8:00 AM. This nighttime period provides the most consistent window for observing temperature differentials.

5.1.2 Soil Temperature Data. In all five scans, the soil differentials monitored at level 9 follow a smooth, sinusoidal configuration, reaching maximum values around noon and minimum values between 8:00 and 10:00 PM. In the first three scans, the curves remain negative at all times, though there is a gradual upward movement. Soil temperatures in scans 4 and 5, while showing the same configuration, now reach into the positive zone of the graph. Further inspection of the temperature data in Chapter 4 (Figures 4.2 to 4.11) indicates that the soil is gradually cooling. During scan number 1, the soil temperatures decreased

with depth. By scan 4, however, this trend was reversed. This shows that the soil has changed from a net energy absorber to a net energy emitter. This is reflected in the positive values of the soil differential curves in scans 4 and 5 (Figures 5.4 and 5.5).

## 5.2 Thermal Imagery

Figures 4.12 to 4.14 show the progression of images of the experimental slab produced on August 26, 1980. Figure 4.12, taken at 6:30 AM, one-half hour before sunrise, shows clear temperature differentials that exactly correspond to the location of Voids 1 and 3. Void 2, on the west edge, is not evident due to the edge effect, which is discussed in Chapter 4.

The darker shade of the slab above the voids means that the surface is cooler. The thermistor data taken at that moment also show the voids to be an average of  $0.8^{\circ}\text{F}$  ( $0.4^{\circ}\text{C}$ ) cooler than the rest of the slab (see Figure 5.2).

Images taken after sunrise (Figures 4.13 and 4.14) show that same general pattern of surface temperatures. However, the clarity of the images is obscured by the shadows of the equipment shelters and by some localized solar reflection. It is interesting to note the generally darker shade of the slab in the area that was in shadow in the early morning hours. This momentary, uneven heating of the

slab caused a permanent trace to be made that corresponds to the area of daily shadows. The areas of higher solar reflection (showing very white) are in areas where the surface is slightly rougher. This roughness decreases the emissivity of the surface, thereby increasing the reflectivity. Despite these mitigating circumstances, however, the voided areas are still showing cooler surface temperatures. The thermistor data for August 26, 1980, (Figure 5.2) show the void surfaces to be between 0.7 and 1.2<sup>o</sup>F (0.4 to 0.7<sup>o</sup>C) cooler than the rest of the slab during the time of the infrared scans.

The sensitivity range of the Texas Instruments RS-310 Infrared System, used in this study, is 0.3<sup>o</sup>F (0.15<sup>o</sup>C). The Bendix Thermal Mapper, used in the earlier study, has a sensitivity range of 0.45<sup>o</sup>F (0.25<sup>o</sup>C) (see Appendix 1). Using the  $\pm$  0.45<sup>o</sup>F value as the lower bound of the detectable region, Table 5.1(a) was compiled to illustrate the percentage of time that the observed temperature differentials could be detected by IRT during the five scans included in this study. The total time of the thermistor scans was 150 hours. The temperature differentials have been broken into the four regions shown below:

Undetectable	0-0.45 <sup>o</sup> F	(0-0.25 <sup>o</sup> C)
1-3x Range	0.45-1.35 <sup>o</sup> F	(0.25-0.75 <sup>o</sup> C)
3-6x Range	1.35-2.70 <sup>o</sup> F	(0.75-1.50 <sup>o</sup> C)
6-8x Range	2.70-3.60 <sup>o</sup> F	(1.50-2.00 <sup>o</sup> C)

TABLE 5.1 Percentage of Time that Temperature Differentials can be Detected.

Scan	Total Time, hr.	Undetectable, hr.	1-3x Range, hr.	3-6x Range, hr.	6-8x Range, hr.
1	19	4	8	7	-
2	16	7	9	-	-
3	23	14	9	-	-
4	48	14	23	11	-
5	44	3	14	22	5
Total	150	42	63	40	5
%	100	28	42	27	3

(a) Total time

Scan	Night Time, hr.	Undetectable, hr.	1-3x Range, hr.	3-6x Range, hr.	6-8x Range, hr.
1	8	1	5	2	-
2	10	5	5	-	-
3	8	8	-	-	-
4	24	6	15	3	-
5	23	3	7	12	1
Total	73	23	32	17	1
%	100	32	44	23	1

(b) Night time

Based on this comparison, the temperature differentials observed in this study are shown to be within the detectable range of state-of-the-art IRT scanners 72 percent of the time.

It is notable that the best IRT image was produced before sunrise. The interference posed by solar reflection and shadows renders IRT daylight scans harder to evaluate. For this reason, nighttime scans are considered to be more practical. Table 5.1(b) shows that temperature differentials are within the detectable range 68 percent of the time during the night. Further analysis of Figure 5.6 and Table 5.1(b) indicates that the optimum time for IRT scans will generally be between midnight and sunrise.

### 5.3 Correlations with Theory

The theoretical analysis made in Chapter 2 predicts the effect of a void on surface temperatures under steady-state, ideal circumstances. The final hypothesis is made that the surface above a void will be hotter during the day, when the adjusted air temperature is higher than the soil temperature. Conversely, the surface above the void will be cooler during the night, when the air temperature is less than the soil temperature. The transition will occur when the soil and air temperatures are equal. This pattern will follow a sinusoidal configuration with a positive peak around noon and a negative peak around midnight.

The observed results of the surface temperature differentials do not show this idealized situation to be completely valid under real conditions. Roughly sinusoidal variations in differential temperatures are observed at all levels. The shift forward in the time of occurrence of the peak values is attributed to the dynamic temperature conditions that prevail under actual circumstances. This dynamic condition was not accounted for in the steady-state model.

The five curves in Figures 5.1 to 5.5 indicate that the positive peak temperature differential will occur in the late afternoon or early evening, with a corresponding peak negative value in the early morning hours before and after sunrise. This indicates a six to eight hour forward shift in the differential curves that can be attributed to the dynamic temperature conditions.

The soil temperatures monitored confirm the hypothesis made in Chapter 2 that less heat energy will be transferred to the soil below the void than to the soil in the solid areas. This has proven to be a significant factor affecting the surface temperature differentials.

This page replaces an intentionally blank page in the original.

-- CTR Library Digitization Team

## CHAPTER 6. CONCLUSIONS AND RECOMMENDATIONS

The study described in this report was a preliminary investigation to determine whether the surface temperature pattern detected by infrared thermography can be correlated to the location of voids at the pavement/subbase interface. The study has included a theoretical analysis and accumulated actual temperature data to clarify the heat transfer mechanisms involved in the pavement systems.

### 6.1 Conclusions

The conclusions drawn from this study are as follows:

1. Thin voids, 1/8-in. (3-mm) thick, at the pavement/subbase interface have an observable effect on the concrete surface temperatures.
2. The temperature differentials produced by these voids can be detected 72 percent of the time by modern IRT systems. During the late summer/early fall, the magnitude of these temperature differentials is as much as eight times the sensitivity of the IRT systems used.
3. The best time to perform IRT scans is during the night, between 12:00 midnight and sunrise. Consistently high temperature differentials were monitored at night. These differentials were detectable 68 percent of the time. Furthermore, solar reflection and shadows have no bearing on nighttime scans.

4. The shape of the temperature differential curve is variable. It is subject to change from sudden shifts in environmental conditions (from high winds or precipitation) as well as from the more gradual seasonal changes in air and soil temperatures. These changes must be continually observed to predict when temperature differentials will be detectable by IRT.

## 6.2 Recommendations

This study has been preliminary in nature. As such, it has identified potential activities in the detection of voids using infrared thermography. The potential economic benefits to be gained by the undersealing of rigid pavements to avoid punch-out type failures is considerable. However, before IRT can be judged capable of detecting voids under actual conditions, further studies must be conducted.

These further studies should include:

1. Monitoring of the experimental slab in this study should continue for a period of one year. This will effectively quantify the magnitude of and optimum time to measure the temperature differentials.
2. In conjunction with this continuing experiment, scans should be conducted on sections of actual pavements where voids are thought to exist. Data accumulated from the experimental slab should be used to predict the optimum times for the actual field studies.
3. Where suspected voids are located in the field, the pavements should be cored to verify the existence of voids.
4. After verifying the existence of voids, the pavements should be undersealed.

5. IRT scans should then be performed to verify the effectiveness of the undersealing.
6. A computer program to predict temperature differentials under different environmental conditions should be formulated. This program should be designed to account for both the short-term and long-term dynamic temperature patterns occurring in real-life situations.
7. Work should be begun on the development of a more practical and economical IRT system. The systems used in this study are airborne scanners. These scanners exhibit many features peculiar to that use. Certain features could be modified or dropped altogether, yielding a system especially made for use in low-level IRT scans.

This page replaces an intentionally blank page in the original.

-- CTR Library Digitization Team

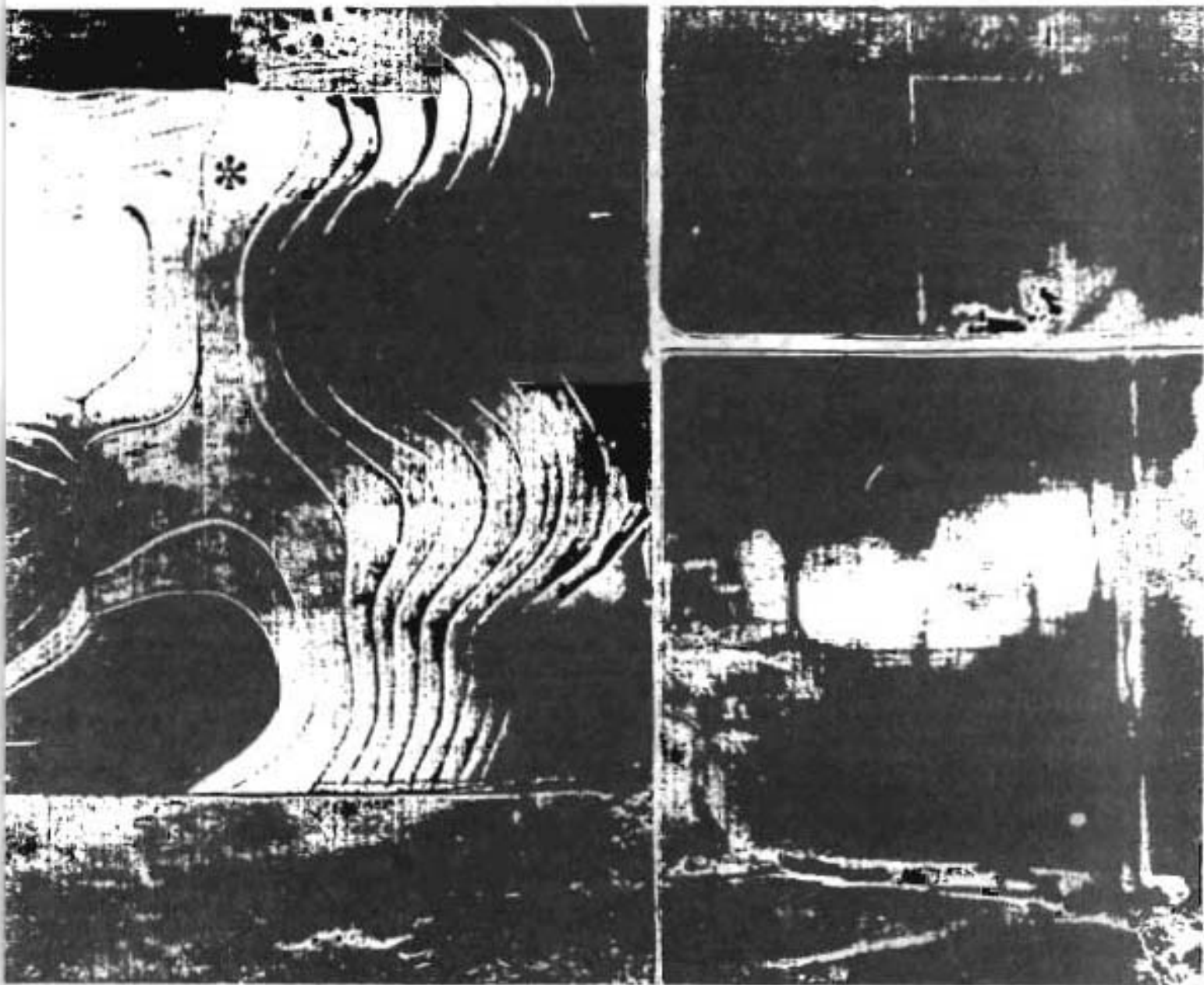
**APPENDIX**

This page replaces an intentionally blank page in the original.

-- CTR Library Digitization Team



# RS-310 AIRBORNE INFRARED MAPPING SYSTEM



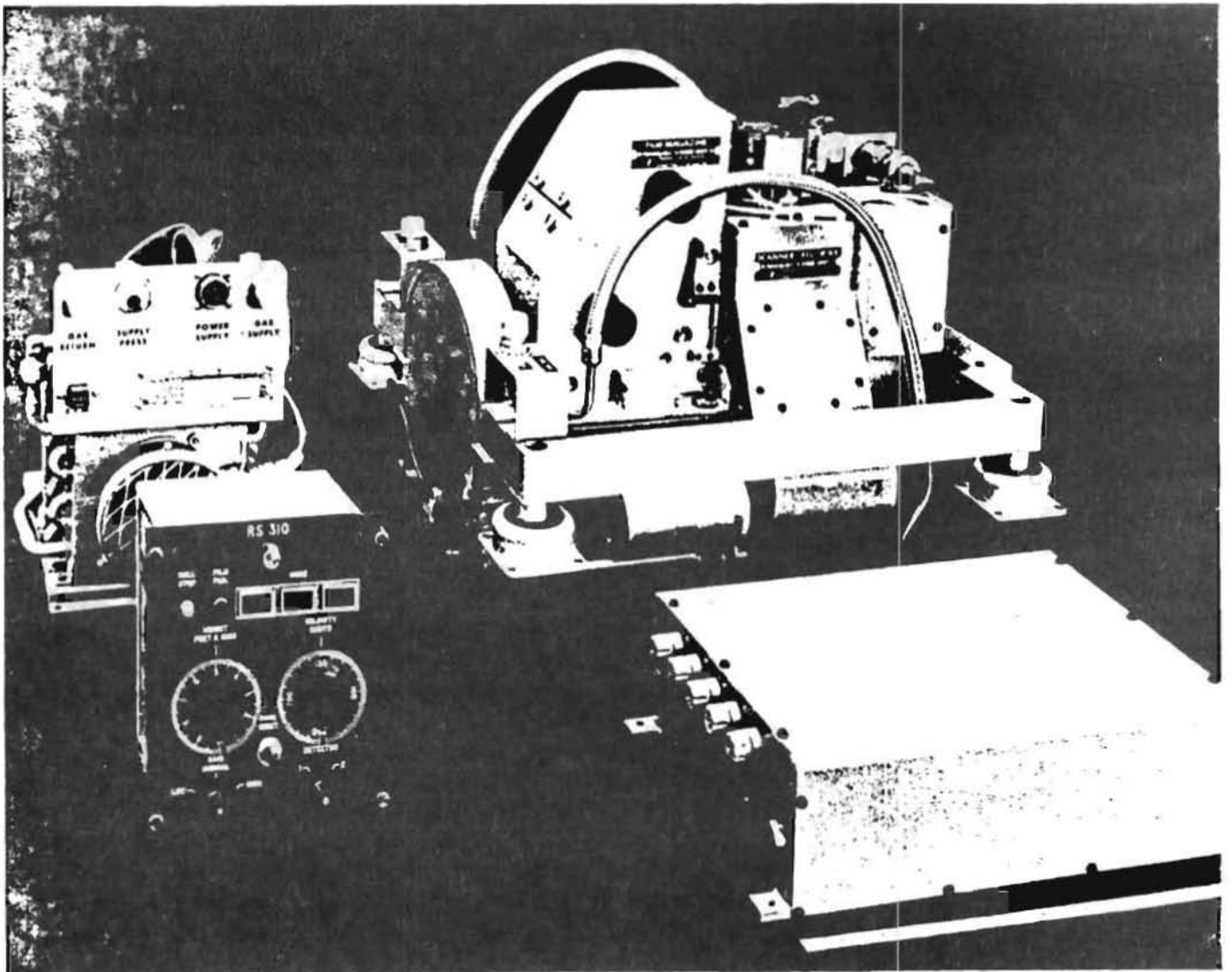
\* Utility line buried in 1968, approximately 3-feet deep



TEXAS INSTRUMENTS  
INCORPORATED

## AIRBORNE MAPPER □

The RS-310 is a passive, airborne infrared imaging system that scans the ground along and to both sides of the flight path and produces a continuous image of the scanned terrain. Energy is received by the scanner from the ground, focused on cryogenic-cooled detectors, converted to light through the use of a light-emitting diode, and by means of a mechanically-coupled recorder exposes the photographic film in the film magazine. The film is moved at a rate proportional to the velocity and height of the aircraft, producing the continuous photographic record of the radiant energy detected.



## OPERATIONAL SPECIFICATIONS

Texas Instruments collective knowledge and expertise acquired through broad experience in the field of military infrared sensors and in the NASA earth resources program was used to design the RS-310 to meet the needs of the earth resources and remote sensing industry. The parameters of the RS-310 are shown below.

<b>Resolution (milliradians)</b>	<b>1.0 (Minimum)</b>
<b>Field of view (degrees)</b>	<b>90</b>
<b>V/H range (radians/second)</b>	<b>0.03 to 0.2 (at 1 milliradian, 0.3 at 1.5 milliradian)</b>
<b>Noise equivalent temperature (1 milliradian)</b>	<b>0.20 (InSb) (Maximum) 0.15 (HgCdTe) (Maximum) °C</b>
<b>Scanner RPM</b>	<b>3000 (200 scans/sec.)</b>
<b>Detector types</b>	<b>InSb, and/or HgCdTe; or Si; or GeHg; or photomultiplier tube</b>
<b>Wavelength region (micrometers)</b>	<b>0.3 - 14 (Optical capability)</b>
<b>Detector cooling</b>	<b>Liquid nitrogen with greater than 6-hour hold time (Closed-cycle cooling optional)</b>
<b>Collecting aperture (inches<sup>2</sup>)</b>	<b>6.35</b>
<b>Roll stabilization</b>	<b>±10°</b>
<b>Number of units in system</b>	<b>4</b>
<b>Size and weights of units</b>	
<b>Scanner/recorder (Unit 1)</b>	<b>16.50" L x 14.50" W x 15.00" H 50 lbs. (without magazine)</b>
<b>Control panel (Unit 2)</b>	<b>5.75" L x 5.32" W x 3.00" H 2.7 lbs.</b>
<b>Power supply (Unit 3)</b>	<b>13.00" L x 8.50" W x 3.75" H 11.4 lbs.</b>
<b>Film magazine (Unit 4)</b>	<b>6.40" L x 5.925" W x 8.45" H 9.0 lbs. (without film)</b>
<b>Total system volume (ft.<sup>3</sup>)</b>	<b>3.0</b>
<b>Total system weight (lbs.)</b>	<b>73.1</b>
<b>Power requirements</b>	
<b>115 Vac, 3 phase, 400 Hz</b>	<b>100 VA</b>
<b>28 Vdc</b>	<b>135 Watts</b>

## FUNCTIONAL DESCRIPTION — BENDIX THERMAL MAPPER

### 2.1 GENERAL DESCRIPTION OF THE BENDIX THERMAL MAPPER

The information provided in Sections 2.1 through 2.11 is specifically applicable to the Model LN-2 Thermal Mapper. Sections 2.2 and 2.5 through 2.11 are also applicable to the other mapper models, i.e., LN-1, LN-3, and CCC-1. Those areas of the other models that differ from the LN-2 model are described under Sections 2.12 through 2.14.

The Bendix LN-2 Thermal Mapper, pictured in Figure 2-1, is described in the system diagram, Figure 2-2. The nominal performance is specified in Table 2-1; actual performance, which is recorded in the respective Log Book, meets this minimum performance. The electrical schematic is shown in Figure 7-1.

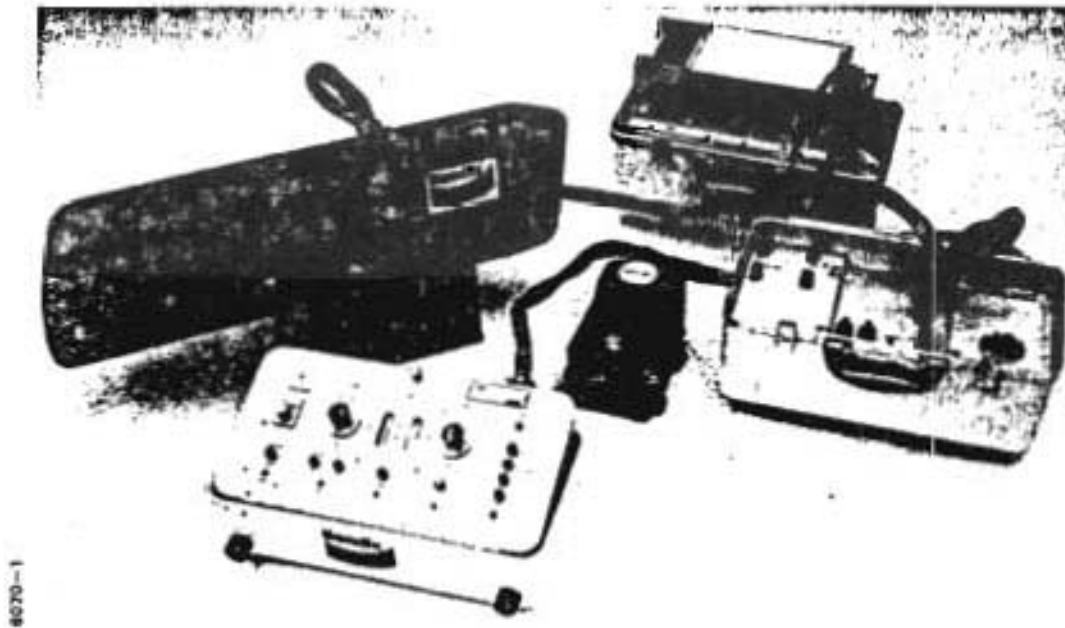


Figure 2-1 Bendix Thermal Mapper

The thermal mapper consists of two major assembly packages, the Scan Head Assembly (P/N2303551) and the Control Console and Power Supply Assembly (P/N2336036). The two assemblies are connected by two cables and a single power cable for the external 28 VDC power.

The scan head is further defined by the Scanner Schematic, Figure 2-3. Each of the sub-assemblies of the mapper is discussed herein.

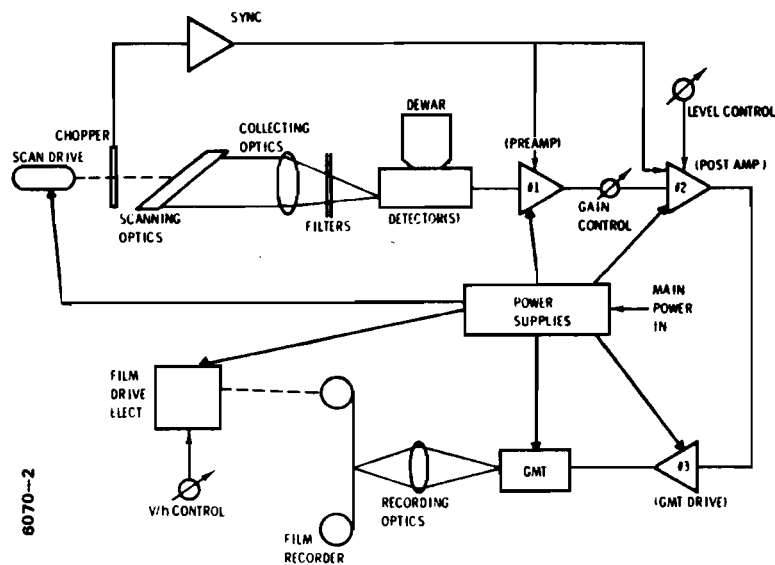


Figure 2-2 Thermal Mapper System Diagram

TABLE 2-1

LN-2 THERMAL MAPPER SPECIFICATIONS

<u>Operating Times</u>	
Film Running Time	1.5 hr at max V/h 3.0 hr or more at average V/h
Liquid Nitrogen Hold Time	3.5 hr
<u>Performance</u>	
Instantaneous Field-of-View (resolution)	2.5 milliradians
Lateral Scan Angle	120 degrees
Temperature Difference Sensitivity	
Total Available Spectral Coverage	
(Manual setting of choice of one of four filters available in flight.)	
Maximum V/h for Continuous Scan (aircraft velocity in fps/altitude in feet)	0.250 radians/sec or 150 knots/1000 ft dial indication
Standard Detector	Indium Antimonide
Detector Cooling	Liquid Nitrogen
Power Requirements (with roll compensation)	10 amp @ 26 to 28 VDC
Scan Head Weight	35 lb
Control Electronics Weight	20 lb
Recording Medium	70-mm RAR 2498 Recommended
Film Capacity	150 ft

See following page

The possible uses of this module cover the extremely wide dynamic range from unfiltered reflected sunlight to twilight conditions. To accept the maximum signal while retaining the capability of making imagery under very low level conditions, it is necessary to attenuate the large signals. Your module is equipped with a 1.0 "neutral density" Wratten filter. If low-level measurements are required, or if other filtering is desired, this filter must be removed. The filter is located in a small, threaded housing screwed into the "snout" of the module. It can be removed using a coin as a screwdriver. The small housing is made of hardened steel and is designed for use as a cutting tool to cut plastic filter material.

#### 2.12.4 Mercury-Cadmium-Telluride Module

Utilizing an advanced semiconductor technology, this module makes data collection in the 8- to 14- $\mu$  atmospheric window possible with only liquid nitrogen cooling.

Figure 2-15 is the range of spectral sensitivity of the long-wavelength module. A filter is necessary for operation in the 8- to 14- $\mu$  window to remove the effects of shorter wavelengths (including the visible and reflected IR regions). Filtered operation in the 4.0- to 5.5- $\mu$  range is also possible, although the InSb module has much better sensitivity at this wavelength. A sensitivity of 0.25°C is guaranteed with this module when filtered from 8 to 14 $\mu$ . No guaranteed figure is given for 4.0- to 5.5 $\mu$  operation.

Handling precautions and other operational considerations are the same as for the InSb module. Schematics of the circuitry used with this module (Figures 7-4 and 7-5) are given in the Maintenance Section.

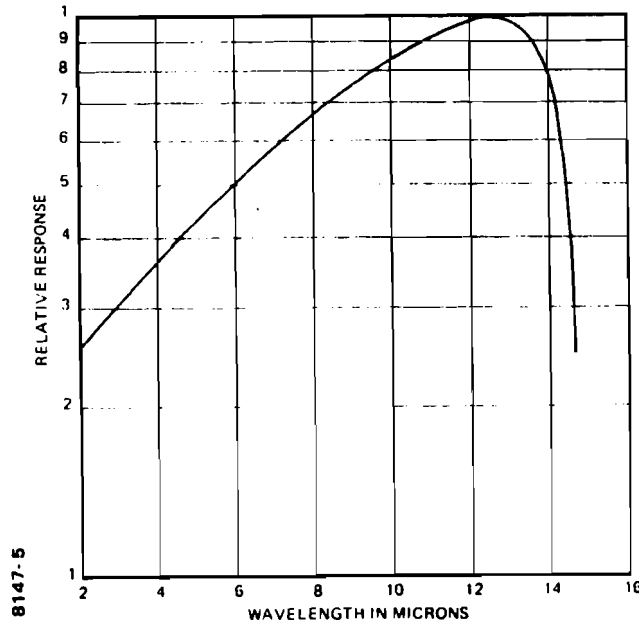


Figure 2-15 HgCdTe Spectral Response Curve

## REFERENCES

1. American Society of Heating, Refrigerating and Air-Conditioning Engineers, HVAC-Guide 1960, pp. 108-134.
2. Birkhoff, John, and McCullough, B. Frank, Detection of Voids Underneath Continuously Reinforced Pavements, Center for Highway Research, The University of Texas at Austin, Report No. 177-18, August 1979, pp. 1-3.
3. Bukowski, Mark E., "Infrared Thermography for the Detection of Voids Between the Subbase and Concrete Pavements," unpublished paper, December 1979, pp. 5-6.
4. Hazard, William R., and Underwood, Stephan A., "Modeling Heat Loss With Aerial Thermography," January 1979, p. 23.
5. Holt, F.B., and Manning, D.G., Infrared Thermography for the Detection of Delaminations in Concrete Bridge Decks, 4th Biennial Infrared Information Exchange, August 1978, pp. 3-5.
6. Jong, Bartele de, Net Radiation Received by a Horizontal Surface at the Earth, Delft University Press, 1973, p. 9.
7. Rowley, Frank B., and Algren, Axel B., Thermal Conductivity of Building Materials, University of Minnesota, 1937, p. 40.
8. Sowan, F.A., Applications of Infrared Detectors, Mullard Limited, 1971, pp. 1-2.
9. Urban, Lloyd Victor, A Laboratory Investigation of Temperature and Velocity Fields in a Stratified Cooling Reservoir, Dissertation, The University of Texas at Austin, December 1971, pp. 41-48.

10. U.S. Department of Transportation, Federal Highway Administration, Highway Statistics 1974, pp. 199, 215, 228.
11. Wise, John R. and Hudson, W. Ronald, An Examination of the Expansive Clay Problem in Texas, Center for Highway Research, The University of Texas at Austin, Report 118-5, July 1971, p. 2.